

A tunable Josephson platform to explore many-body quantum optics in circuit-QED

Javier Puertas Martínez,¹ Sébastien Léger,¹ Nicolas Gheeraert,¹ Rémy Dassonneville,¹

Luca Planat,¹ Farshad Foroughi,¹ Yuriy Krupko,¹ Olivier Buisson,¹ Cécile

Naud,¹ Wiebke Guichard,¹ Serge Florens,¹ Izak Snyman,² and Nicolas Roch¹

¹*Univ. Grenoble Alpes, CNRS, Grenoble INP, Institut Néel, 38000 Grenoble, France*

²*Mandelstam Institute for Theoretical Physics, School of Physics,
University of the Witwatersrand, Johannesburg, South Africa*

The quest to understand and control the interactions between light and matter has a distinguished history, stretching back to the ray optics of Euclid and Ptolemy. In recent decades, physicists have been able to hone in on the quantum scale. Coupling an isolated emitter to a single mode of the electromagnetic field is now routinely achieved in the laboratory¹, and standard quantum optics provides a complete toolbox for describing such a setup. Current efforts aim to go further and explore the coherent dynamics of systems containing an emitter coupled to several electromagnetic degrees of freedom²⁻⁸. Combining superconducting metamaterials and qubits could allow for the observation of genuinely macroscopic quantum effects such as a giant Lamb shift⁹ or non-classical states of multimode optical fields¹⁰⁻¹³. In this work, we couple a transmon qubit to a high impedance, centimeter-scale, metamaterial¹⁴ waveguide, made of 4700 in-situ tunable Josephson junctions. Our device combines three essential properties required to go beyond the standard quantum optics paradigm and reach the multi-mode, many-body regime, namely: a tunable waveguide with a high density of electromagnetic modes^{15,16}, a qubit non-linearity comparable to the other relevant energy scales, and ultrastrong coupling¹⁷⁻²⁰ between the qubit and the waveguide modes. Besides providing experimental evidence for these non-trivial requirements, we also develop a quantitative theoretical description that does not contain any phenomenological parameters and that accurately takes into account vacuum fluctuations of our large scale quantum circuit in the regime of ultrastrong coupling and intermediate non-linearity. Furthermore, we show that the influence on the transmon of our fully controllable on-chip environment well approximates that of the macroscopic bath envisioned in the celebrated work of Caldeira and Leggett²¹. Our work demonstrates that Josephson waveguides offer a promising platform to explore many-body quantum optics in a controlled way.

Due to strong interactions between elementary constituents, correlated solids²² and trapped cold atoms²³ host fascinating many-body phenomena. Attempts to produce similar effects in purely optical systems are ham-

pered by the obvious fact that photons do not naturally interact with each other. If this obstacle can be overcome, there is the tantalizing prospect of probing the many-body problem using the contents of the quantum optics toolbox, such as single photon sources and detectors, high-order correlations in time-resolved measurements, entanglement measures, and phase space tomographies to name a few.

One route to building a many-body quantum optical system is to rely on arrays of strongly non-linear cavities or resonators²⁴⁻²⁶, but minimising disorder in such architectures is a formidable challenge. Another route that circumvents these difficulties involves coupling a single well-controlled non-linear element to a disorder free harmonic environment. If the difficult experimental challenge of engineering an ultra-strong coupling can be overcome, thus exceeding the boundaries of the standard single photon regime in quantum optics, this approach could pave the way to bosonic realizations of electronic impurity systems such as the famous Kondo and Anderson models²⁷. Our goal here is to achieve a large coupling between a sufficiently non-linear qubit and a quantum coherent environment containing many harmonic degrees of freedom.

When coupling an impurity to a finite size electromagnetic environment, five important frequency scales have to be considered. The impurity is characterized by its qubit frequency ω_{qubit} , i.e. the excitation frequency between its two lowest internal states. Real impurities always possess more than two levels. The anharmonicity α , defined as the difference between ω_{qubit} and the frequency for excitation from the second to third internal impurity state, characterises the departure of an impurity from a trivial harmonic oscillator ($\alpha \rightarrow 0$) or a pure two-level system ($\alpha \rightarrow \infty$). The coupling between the impurity and environment is characterized by the spontaneous emission rate Γ at which the impurity exchanges energy with its environment. The environment itself is characterized by its free spectral range $\delta\omega$, which measures the typical frequency spacing between environmental modes, and the spectral broadening κ of these modes due to their coupling to uncontrolled degrees of freedom. The sought-after multi-mode regime is obtained when Γ is larger than $\delta\omega$ so that the impurity is always coupled to several discrete environmental modes, producing a cluster of hybridized qubit-environment resonances. There are several requirements for reaching the many-body regime. First, Γ must be a significant fraction of ω_{qubit} (ultra-

strong coupling). This is a prerequisite for multiparticle decay^{10,13}. If the coupling is too weak, the system becomes trivial, since only number-conserving processes are relevant (Equivalently Markov and rotating wave approximations apply.) A second requirement is $\alpha \gtrsim \Gamma$. If this condition is not met, the non-linearity of the impurity is swamped by the broadening of the impurity levels, and the same frequency will drive transitions between several impurity levels, so that the system as a whole behaves more like a set of coupled harmonic oscillators than like a two-level system coupled to an environment²⁸. Within the many-body regime, two limits can be distinguished. In the case of a finite-size environment that we address here (namely, $\delta\omega > \kappa$), each mode of the system can be addressed and controlled individually, while in the limit of a thermodynamically large environment ($\delta\omega/\kappa \rightarrow 0$) one recovers a smooth dissipation-broadened qubit resonance.

The multi-mode ultra-strong coupling regime (defined by the first two conditions above) is hard to reach in quantum optics experiments because the coupling to three-dimensional vacuum fluctuations arises at order $[\alpha_{\text{QED}}]^3$, with $\alpha_{\text{QED}} \simeq 1/137$ the fine structure constant¹. However, for superconducting qubits coupled to transmission lines, the scaling is much more favorable^{11,29–31} than in a vacuum. Indeed the ratio $\Gamma/\omega_{\text{qubit}}$ can essentially be made arbitrarily large, provided the impedance of the environment matches that of the qubit (see Sec. E of the Supplementary Information). Building on this ability of superconducting circuits to reach very large couplings, several experiments demonstrated the ultra-strong coupling regime in coupled qubit/cavity systems^{17–19,32}. The rich physics associated to this coupling regime has also been evidenced using quantum simulation^{33,34}. The condition $\Gamma > \delta\omega$ has also been fulfilled by coupling superconducting qubits to open transmission lines^{35–37} or engineered resonators^{2,4}. However, it is only recently that the necessary conditions for the many-body regime were demonstrated concurrently^{6,7}. The device of Refs. 6 and 7 consists of a flux qubit coupled to the continuum provided by a superconducting transmission line, which realises the thermodynamic limit ($\delta\omega/\kappa \rightarrow 0$). Limitations of such setups include the lack of a microscopic model (since it is hard to characterize the waveguide properties of a transmission line outside the relatively narrow 4-8 GHz band where microwave transmission experiments can comfortably be performed), and importantly, that the transmission line is not an in-situ tunable environment.

In this work, we circumvent the above limitations, by designing circuits that provide independent tunability of both a qubit and a finite size but very large environment, while allowing high-precision spectroscopic measurements of the environment itself ($\delta\omega > \kappa$) and first principle modeling. Our device, shown in Figure 1b, consists of a transmon qubit, which is relatively insensitive to both charge and flux noise, capacitively coupled to a long one-dimensional Josephson metamaterial, com-

prising 4700 SQUIDs. Such chains have been studied since the early 90's in the context of the superconductor-insulator transition^{38–41} or to explore dual of the Josephson effect^{42–44}. Our setup differs in two ways from these previous works. First, we took great care to produce a chain in the linear regime, far from the onset of non-linear effects such as quantum phase slips⁴⁵, so that one of the basic benefits of quantum optics, i.e. the elimination of non-linearities where they are not wanted, is realized. Second, we performed AC microwave spectroscopy of our device, instead of DC transport measurements. This allows us to characterize the electromagnetic degrees of freedom, also called *Mooij-Schön* plasma modes^{28,46–50}, microscopically. We managed to resolve as many as 50 individual low frequency electromagnetic modes of this non-dissipative and fully tunable environment (See Figure 2c). An essential property of the Josephson metamaterial is its high characteristic impedance $Z_c = \sqrt{L_J/C_g} \simeq 1590 \Omega$, which being of the same order of magnitude as the effective impedance of our transmon qubit, $Z_T = \hbar/(2e)^2 \sqrt{2E_{C,T}/E_{J,T}} \simeq 760 \Omega$ (here at zero flux), allow us to reach multi-mode ultra-strong coupling. The simplicity of the transmon architecture enables us to either compute from first principles or to extract all the parameters necessary to construct a microscopic model of the full system, without dropping the so-called ‘ A^2 -terms’, a routine approximation in optics^{51–55}, that however breaks down at ultra-strong coupling.

Our measurements are based on the frequency-resolved microwave transmission through the whole device. Figure 2b shows the amplitude of the transmitted field at a fixed value of the external magnetic field, and at low probe power. This spectrum reveals a set of resonances in our device, displaying a narrow spectral broadening $\kappa/2\pi = 20\text{MHz}$ (for the non hybridized modes of the chain) caused by the coupling to the 50Ω contacts. As the external magnetic field is varied, two modulation periods are seen in the resonance spectrum (Figure 2a). The short and long periods correspond respectively to a one quantum $\Phi_0 = h/2e$ increase of the flux through the large transmon or through the small chain SQUID loops. This feature allows us to adjust independently the flux threading the transmon SQUID loop (Φ_T) from the one threading the chain SQUID loops (Φ_C). The former controls the qubit frequency, while the latter controls the impedance of the environment, and hence the qubit-environment coupling strength. Before studying the hybridization between the transmon and chain, we characterize the chain on its own by setting $\Phi_T = \Phi_0/2$, so that the qubit decouples from it (See Fig. 2c and Sec. B of the Supplementary Information). We obtain a good fit between the dispersion relation predicted by a microscopic model and the one extracted from the measured resonances. This allows us to extract all of the parameters necessary to characterize the chain modes.

The transmon qubit becomes active when $\Phi_T \neq \Phi_0/2$, and is expected to hybridize with the chain. Figure 3a

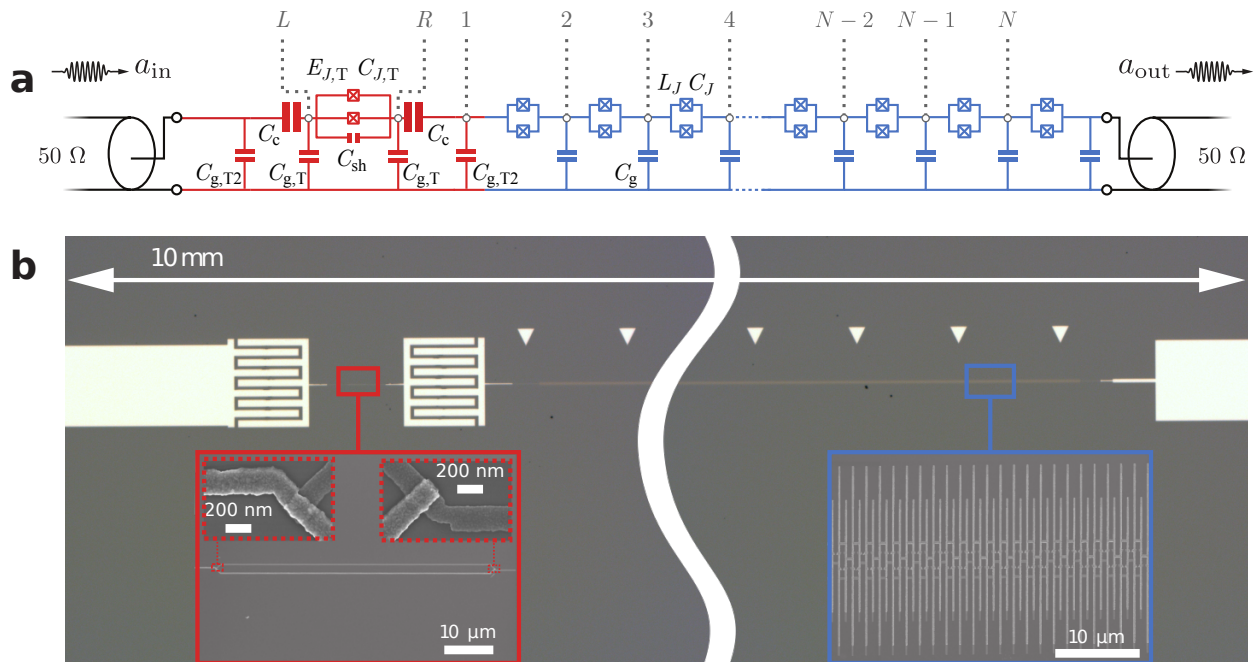


FIG. 1. **A Josephson platform for waveguide quantum electrodynamics.** **a** Lumped element model of the circuit including the nodes used in the calculations. **b** Optical microscope image of the sample. The two zoom-in are SEM pictures of the SQUID of the qubit (red square) and the SQUIDs in the chain (blue square). The qubit is capacitively coupled to the chain and to a 50Ω measurement line, via large interdigital contacts. Only a small portion of the Josephson chain, which comprises 4700 SQUIDs in total, is shown.

shows a low-power spectroscopy of the system as a function of Φ_T , keeping Φ_C nearly constant. When a chain mode is not hybridized with the qubit, the corresponding spectral line runs nearly horizontally. When Φ_T is varied, the qubit frequency sweeps across the resonances of the chain modes and creates a clear pattern of several avoided level crossings (See Figure 3a). We note that at fixed Φ_T , several chain modes in the vicinity of the transmon resonance are visibly displaced. Thus, the transmon simultaneously hybridizes with many modes. This is a signature of multi-mode ultra-strong coupling, a topic that will be further addressed below. Evidence that the transmon behaves as a qubit is provided by its saturation spectrum (Figure 3b). Here the fluxes Φ_T and Φ_C are kept constant, while the transmission through the system is recorded at increasing probe power. For a harmonic system, the resonance positions are independent of driving power. In an anharmonically oscillating classical system, a gradual dependence on the driving power would appear. Experimentally, we observe that below a driving power ~ -10 dBm, the resonance positions in the transmission spectrum are independent of the driving probe power. As the driving power increases beyond -10 dBm, the peak around 4.6 GHz disappears while the other peaks assume the positions they have when the qubit is inactive. (The horizontal lines correspond to the low power spectrum when $\Phi_T = \Phi_0/2$.) This is evidence of saturation, a clear qubit signature^{9,35,36}. The fact that

several chain modes are shifted when the transmon is saturated constitutes an additional proof that the transmon hybridizes with many modes at once.

To quantify the hybridization of the transmon mode with the chain modes, we compare the normal mode spectrum of the full system at $\Phi_T \neq \Phi_0/2$ to the spectrum at $\Phi_T = \Phi_0/2$. As mentioned above, in the latter case, the transmon decouples from the bare modes of the chain. The system with $\Phi_T \neq \Phi_0/2$ therefore has one extra mode in the vicinity of the transmon frequency. We define the relative frequency shift $\delta\phi_n(\Phi_T, \Phi_C)$ as the difference in frequency between the n th mode of the coupled and uncoupled chains, normalized to the free spectral range of the chain $\delta\omega_n(\Phi_T, \Phi_C) = \omega_n(\Phi_0/2, \Phi_C) - \omega_{n-1}(\Phi_0/2, \Phi_C)$, and including a π factor for later convenience, i.e.

$$\delta\phi_n(\Phi_T, \Phi_C) = \pi \frac{\omega_n(\Phi_0/2, \Phi_C) - \omega_n(\Phi_T, \Phi_C)}{\delta\omega_n(\Phi_T, \Phi_C)}, \quad (1)$$

where $\omega_n(\Phi_T, \Phi_C)$ is the frequency of the n th lowest non-zero mode for a given flux in the transmon and in the chain. This frequency shift is readily extracted from the peak positions in our global spectroscopic map (Fig. 2a). Remarkably (see Sec. H of the Supplementary Information for a derivation), $\delta\phi_n(\Phi_T, \Phi_C)$ in Eq. (1) equals the phase shift experienced by mode n due to the presence of the nearby transmon mode:

$$\delta\phi_n(\Phi_T, \Phi_C) = \phi_n(\Phi_T, \Phi_C) - \phi_n(\Phi_0/2, \Phi_C), \quad (2)$$

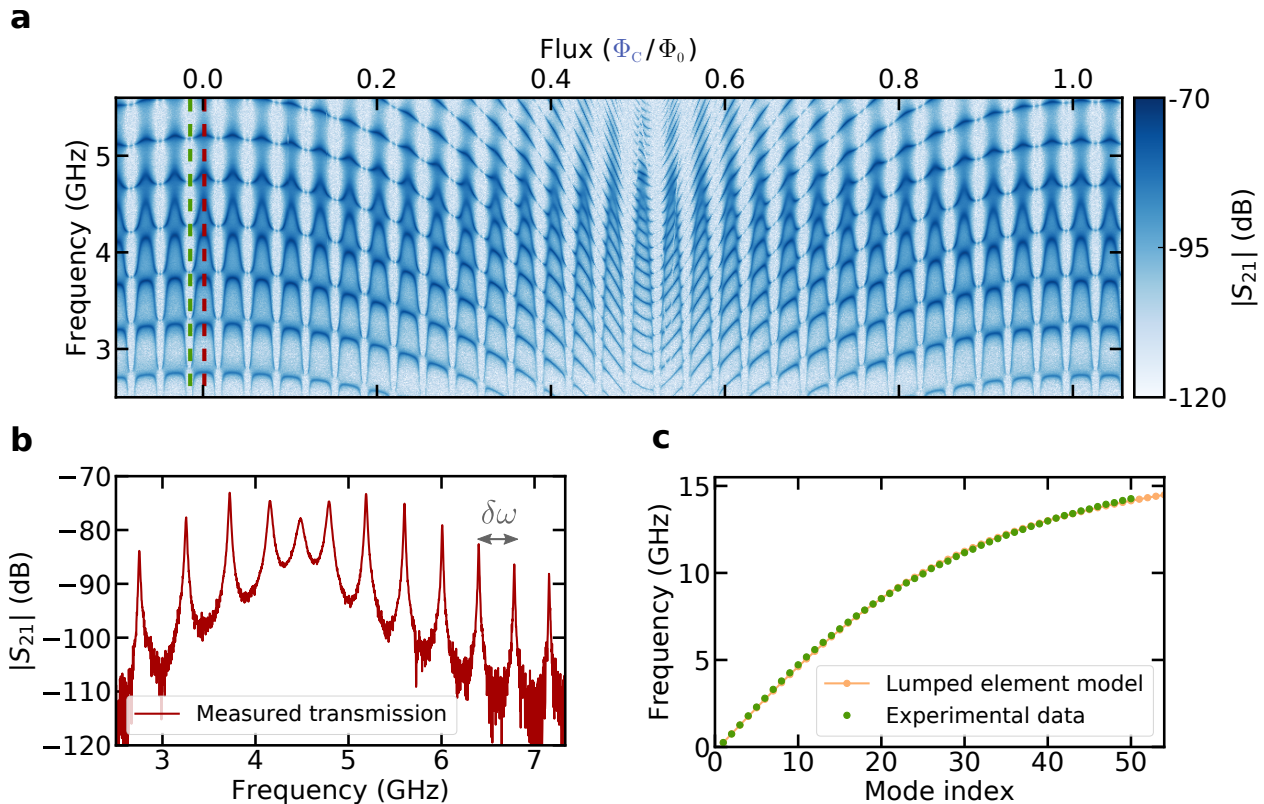


FIG. 2. **Spectroscopic analysis of the full quantum circuit.** **a** Microwave transmission measurement of the complete device (transmon and chain) shown in panel b of in Fig 1, as a function of flux. Two flux periods can be seen, the long one (resp. the short one) being related to the SQUIDs in the chain (resp. in the qubit). Two vertical cuts indicate the spectroscopic traces shown in the two bottom panels respectively. **b** Frequency trace of microwave transmission through the device at flux $\Phi_C = 0$ (red cut in panel a), in which case the transmon flux is also $\Phi_T = 0$. The free spectral range $\delta\omega$ is shown in grey. **c** Dispersion relation of the chain alone obtained from the fit of the resonances at chain flux $\Phi_C = -0.015 \Phi_0$ corresponding to $\Phi_T = -\Phi_0/2$ (green cut in panel a), so that the chain modes do not hybridize with the transmon.

where $\phi_n(\Phi_T, \Phi_C)$ is the phase shift of mode n of the full system at transmon flux Φ_T and chain flux Φ_C . From Eq. (1) it follows that the phase shift equals 0 (resp. π) for modes far below (resp. far above) the renormalized transmon frequency. For hybridized modes in the vicinity of the transmon line, $\delta\phi_n(\Phi_T, \Phi_C)$ lies between 0 and π . This behavior is clearly observed in Fig. 4a where the measured relative frequency shifts are reported for a chain flux $\Phi_C = 0$ and various transmon fluxes Φ_T . The wide frequency dispersion of intermediate $\delta\phi_n(\Phi_T, \Phi_C)$ provides direct evidence for a hybridization with up to ten chain modes. In the thermodynamic limit of an infinite chain with perfect impedance matching to the measurement ports, the transmon-induced phase shift $\delta\phi_n(\Phi_T, \Phi_C)$ becomes a continuous function $\delta\phi(\omega, \Phi_T, \Phi_C)$ of the mode frequency ω . Moreover, it can be shown that the frequency derivative of $\delta\phi(\omega, \Phi_T, \Phi_C)$ matches very precisely the theoretically expected lineshape of the dissipative response of the transmon coupled to an infinite environment. (See Sec. I of the Supplementary Information.) This constitutes a central finding of

our work: the renormalized transmon frequency ω_T and linewidth Γ_T can be directly inferred from a measurement of the phase shifts of the individual modes in the finite bath. In terms of measurement protocol however, there is a sharp difference between the chain mode phase shifts and the qubit response functions. Usually, the qubit response is obtained by observing the transmon, and its environment can be viewed as a black box that combines unmonitored decoherence channels as well as the physical ports used for measurement. This procedure constitutes the usual paradigm in the study of open quantum systems. Our protocol is unusual because information about an open quantum system is obtained by monitoring the discrete modes that constitute its dominant environment.

We finally turn to a quantitative analysis of our data, including a comparison to the predictions of a microscopic model, in order to determine if the requirements for reaching the many-body regime has been met. By extracting the maximum renormalized transmon frequency $\omega_{T,\max}$ extracted from the phase shift data of Fig. 4a at chain flux Φ_T an integer multiples of Φ_0 , we are able

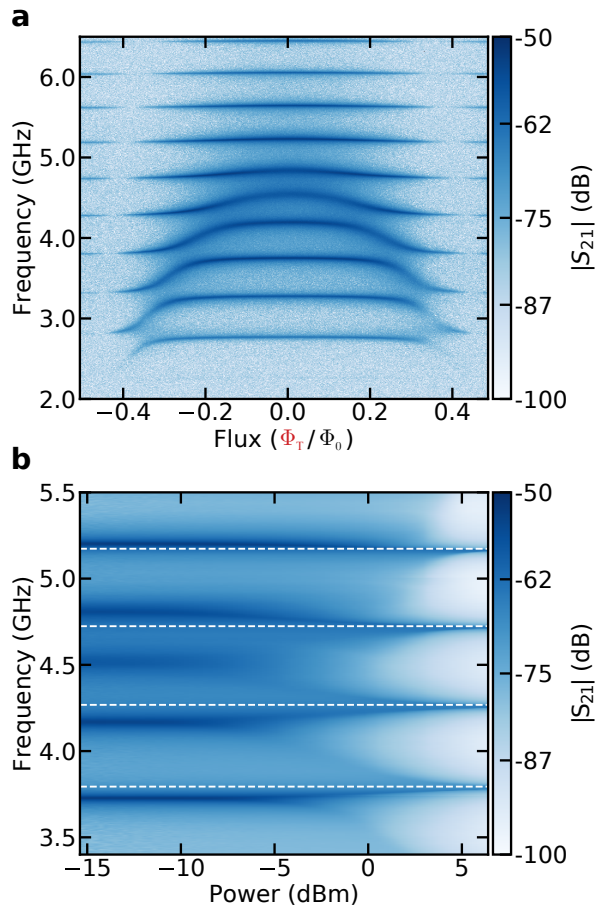


FIG. 3. **Hybridization of qubit and chain modes.** **a** Transmission spectrum as a function of transmon flux Φ_T , at chain flux $\Phi_C \simeq 0$ (representing a small portion of the full spectroscopy in Fig. 2a). The horizontal lines are the chain modes far from the qubit resonance. The flux modulation of the transmon frequency produces a bell-shaped succession of anticrossings. **b** Transmission spectrum as a function of applied microwave power at fixed fluxes $\Phi_T = \Phi_C = 0$. The white dashed lines indicate the modes of the array at $\Phi_T = \Phi_0/2$. With increasing power, the transmon-like mode near 4.5 GHz disappears, showing its non-linear quantum character. In addition the modes of the array shift to their bare frequencies.

to infer the only remaining unknown system parameter, namely the maximum transmon Josephson energy $E_{J,T,\max}$. This allows us to estimate the anharmonicity of the transmon α , which ranges from 0.36 GHz at $\Phi_T = 0$ to 0.44 GHz at $\Phi_T = 0.3\Phi_0$. We emphasize that the condition $\alpha \gtrsim \Gamma_T$ for anharmonic many-body behavior is thus fulfilled (see Fig. 4b for the extracted transmon linewidth Γ_T , which lies in the range 0.2-0.4GHz). Using the extracted parameters to calculate $\delta\phi(\omega, \Phi_T, \Phi_C)$ according to Eq. (11) we find the predicted theoretical lines in Fig. 4a. The excellent agreement between theory and experiment seen here for six different values of Φ_T persists for each of the hundreds of (Φ_T, Φ_C) combina-

tions where we have made the comparison. (See Sec. C of the Supplementary Material for a further selection of results.) We stress that this agreement is obtained after all model parameters have been fixed, so that there is no fitting involved in comparing the predicted and measured phase shifts. The quantitative modeling of such a large quantum circuit clearly is an important landmark in the field of open quantum systems. In Fig. 4b we examine the transmon linewidth Γ_T that we extracted from the phase shift data, as a function of chain flux Φ_C for fixed transmon flux $\Phi_T = 0$. Very good agreement (with no fitting parameters) is again obtained with the prediction of our model. These results demonstrate that we can tune the qubit-environment coupling independently from ω_T using the flux in the chain, and that we achieved the ultra-strong coupling in our waveguide, *i.e.* coupling to a large number (here 10) of modes with a sizeable linewidth $\Gamma_T/\omega_T \simeq 0.1$. A hallmark of ultra-strong coupling is the failure of the rotating wave approximation (RWA), as previously discussed in coupled qubit and cavity systems¹⁷. We have examined the consequences of the RWA on our microscopic model (see Sec. J of the Supplementary Information), and found a discrepancy of 100MHz in the transmon frequency ω_T , showing the quantitative relevance of non-RWA terms.

In conclusion, this work provides the first demonstration of multi-mode ultra-strong coupling between a transmon qubit and a large and tunable bath. To obtain full control over the environment, a superconducting metamaterial, comprising 4700 SQUIDs, was employed. Although this quantum circuit contains a huge number of degrees of freedom, we were able to characterise all its parameters in-situ. This allows us to demonstrate unambiguously that our systems meets the three conditions required to reach the many-body regime, namely $\Gamma \gtrsim \delta\omega$, $\Gamma \gtrsim 0.1\omega_{\text{qubit}}$ and $\alpha \gtrsim \Gamma$. A novel experimental methodology was implemented to analyze the qubit properties by means of the extraction of the phase shifts of the environmental modes. Despite the large size of our quantum circuit, we succeeded in providing a fully microscopic model which accounts for the transmon response without any fitting parameters. We also found that the qubit linewidth for the long chain agreed with results in the thermodynamic limit, showing that the finite environment has the same influence on the qubit as a truly macroscopic bath. The further possibility to tune the coupling to the environment in-situ, demonstrated by a 50% flux-modulation of the qubit linewidth, opens the way to controlled quantum optics experiments where many-body effects are fully-developped^{9,10,12,13,56,57}, as well as more advanced environmental engineering for superconducting qubits²⁴.

Methods

Sample fabrication and parameters

The sample was fabricated on a highly resistive silicon substrate, using a microstrip geometry. The ground is defined as the backside of the wafer which was gold-plated, ensuring a good electrical conductivity. Interdigital capacitances were chosen to connect the

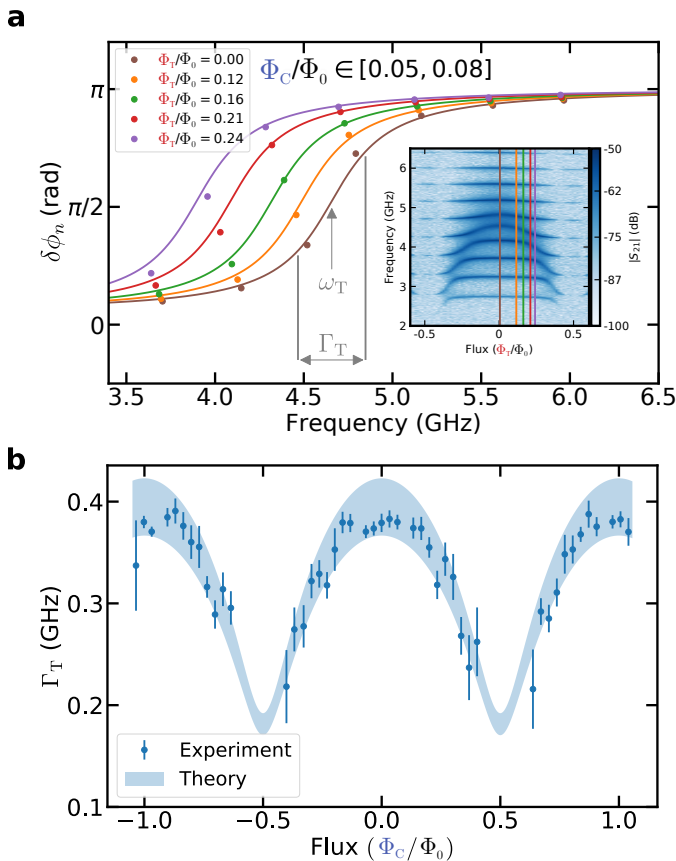


FIG. 4. **Extraction of qubit properties from the measurement of its controlled environment** **a** Phase shift $\delta\phi_n$ of the discrete chain modes as a function of mode frequency ω_n for different transmon fluxes Φ_T , fixing $\Phi_C = 0$. The solid line is a fit using Eq. (2). The inset shows the chosen transmon fluxes Φ_T as line cuts in the transmission measurement (with the same color code). **b** The transmission width Γ_T for different fluxes in the chain Φ_C , showing control of the coupling to the large but discrete environment. The experimental points (dots) are obtained from an arctangent fit of the data in panel a. For better visibility, only the flux values where the transmon frequency is maximum are included. The blue shaded area represents the theoretical expectation for Γ_T , within a confidence interval given by the error in the capacitances in Table I.

transmon and the metamaterial. They do not provide the lowest surface participation factor^{58,59} but they allow us to maximize the coupling capacitances C_c of the transmon to the chain, while minimizing the capacitances to ground $C_{g,T}$ and $C_{g,T2}$. (See panel a of Fig. 1 for the definitions of these capacitances.) This system is probed via two $50\ \Omega$ transmission lines, one of which is capacitively coupled to the transmon, while the other is galvanically coupled to the chain. The whole device (Josephson junctions, capacitances and transmission lines) was fabricated in a single electron-beam lithography step, using a bridge-free fabrication technique⁶⁰. The Josephson elements of the chain are tailored to be deep in the linear regime ($E_J/E_C = 8400$), where E_J and E_C are the respectively the Josephson energy at $\Phi_C = 0$ and the charging energy of a chain element), leaving the transmon as the main source of non-linearity in the system. All parameters of the system are listed in Table I.

Here, $L_{J,\min}$ is the minimum inductance of a chain SQUID loop, (which occurs when $\Phi_C = 0$). There is a slight asymmetry between the two Josephson junctions that constitute a single chain SQUID loop, which is quantified by the asymmetry parameter d . The flux-dependent inductance $L_J(\Phi_C)$ of a chain SQUID loop is given by

$$L_J(\Phi_C) = \frac{L_{J,\min}}{\sqrt{\cos^2(\pi\Phi_C/\Phi_0) + d^2 \sin^2(\pi\Phi_C/\Phi_0)}}, \quad (3)$$

and the corresponding Josephson energy by $E_J(\Phi_C) = \varphi_0^2/L_J(\Phi_C)$ with $\varphi_0 = h/2e$ the reduced flux quantum. The transmon Josephson junctions are symmetric, and hence the flux dependent transmon Josephson energy is given by

$$E_{J,T}(\Phi_T) = E_{J,T,\max} |\cos(\pi\Phi_T/\Phi_0)| \quad (4)$$

The transmon charging energy is not an independent parameter (see Eq. (9)), but is listed in the table, due to the prominent role it plays in what follows. The meanings of the remaining parameters in Table I are explained in panel a of Fig. 1. The majority of the parameter values listed are obtained either using a finite-element solver (Sonnet) or extracted from the measured dispersion relation of the chain at $\Phi_T = 0$. (See Sec. B and D of the supplementary Material.) The only exceptions are C_J , that is obtained from knowledge of the junction areas via an empirical formula, and $E_{J,T,\max}$ that we extract via a procedure described in the last subsection below, which uses the data at Φ_T equal to multiples of Φ_0 in panel a of Fig. 2.

Chain parameters		Transmon qubit parameters	
$L_{J,\min}$	(0.33 ± 0.02) nH	$C_{g,T2}$	(33 ± 1) fF
C_g	(0.13 ± 0.01) fF	$C_{g,T}$	(48 ± 2) fF
C_J	(259 ± 14) fF	C_c	(119 ± 2) fF
N	4700	C_{sh}	(6.9 ± 0.1) fF
d (asymmetry)	0.25	$C_{J,T}$	(5.2 ± 0.3) fF
		$E_{J,T,\max}/h$	(10.2 ± 0.4) GHz
		$E_{C,T}/h$	(2.4 ± 0.1) GHz

TABLE I. Sample parameters

Full Model

The circuit diagram for the lumped-element model is shown in Fig. 1. It consists of $N + 2$ nodes, where N is the number of SQUIDs in the chain. To describe the circuit, we use the Cooper pair number operator \hat{n}_j , which gives the number of Cooper pairs in node j , and the superconducting phase operator $\hat{\varphi}_j$, which gives the superconducting phase at node j . They satisfy the canonical commutation relations $[\hat{n}_j, \hat{\varphi}_l] = i\delta_{jl}$ ⁶¹. Here $j, l \in [L, R, 1, 2, 3, \dots, N]$ with L and R referring to the left and right transmon nodes. As explained before, the SQUIDs of the chain are linear inductors, to a very good approximation. We define $\vec{\hat{n}}^T = (\hat{n}_L, \hat{n}_R, \hat{n}_1, \dots, \hat{n}_N)$ and $\vec{\hat{\varphi}}^T = (\hat{\varphi}_L, \hat{\varphi}_R, \hat{\varphi}_1, \dots, \hat{\varphi}_N)$. In this notation, the Hamiltonian of the circuit is given by

$$H = \frac{(2e)^2}{2} \vec{\hat{n}}^T \hat{C}^{-1} \vec{\hat{n}} - \frac{1}{2} \vec{\hat{\varphi}}^T \hat{J} \vec{\hat{\varphi}} - E_{J,T}(\Phi_T) \cos(\hat{\varphi}_R - \hat{\varphi}_L) \quad (5)$$

\hat{C} is the capacitance matrix, such that elements $[\hat{C}]_{jl} = [\hat{C}]_{lj}$ equal the capacitive coupling between the charges on islands j and l . In the same way, elements $[\hat{J}]_{jl} = [\hat{J}]_{lj}$ of matrix \hat{J} contains the Josephson energy that couples the superconducting phase on island j and island l . Both matrices are $(N + 2) \times (N + 2)$. Their explicit forms are given below in Eqs. (6) and (7). In both matrices, the boundary conditions that determine entries (L, L) and (N, N) are obtained by assuming that the nodes to the left of node L and to

the right of node N are grounded.

$$\widehat{C} = \begin{pmatrix} C_0 & -C_{\text{sh},T} & 0 & 0 & 0 & \cdots & 0 \\ -C_{\text{sh},T} & C_0 & -C_c & 0 & 0 & \cdots & 0 \\ 0 & -C_c & C_1 & -C_J & 0 & \cdots & 0 \\ 0 & 0 & -C_J & C_\Sigma & -C_J & \cdots & 0 \\ \vdots & \vdots & \vdots & \ddots & \ddots & \ddots & \vdots \\ 0 & 0 & 0 & 0 & -C_J & C_\Sigma & -C_J & 0 \\ 0 & 0 & 0 & 0 & 0 & -C_J & C_\Sigma & -C_J \\ 0 & 0 & 0 & 0 & 0 & 0 & -C_J & C_\Sigma \end{pmatrix} \quad (6)$$

The elements in the capacitance matrix are given by

$$\begin{aligned} C_0 &= C_c + C_{\text{sh},T} + C_{g,T} \\ C_1 &= C_c + C_J + C_{g,T2} \\ C_\Sigma &= 2C_J + C_g \\ C_{\text{sh},T} &= C_{J,T} + C_{\text{sh}} \end{aligned}$$

$$\widehat{J} = \frac{\varphi_0^2}{L_J(\Phi_C)} \begin{pmatrix} 0 & 0 & 0 & 0 & 0 & 0 & \cdots & 0 \\ 0 & 0 & 0 & 0 & 0 & 0 & \cdots & 0 \\ 0 & 0 & 1 & -1 & 0 & 0 & \cdots & 0 \\ 0 & 0 & -1 & 2 & -1 & 0 & \cdots & 0 \\ \vdots & \vdots & \vdots & \ddots & \ddots & \ddots & \ddots & \vdots \\ 0 & 0 & 0 & 0 & -1 & 2 & -1 & 0 \\ 0 & 0 & 0 & 0 & 0 & -1 & 2 & -1 \\ 0 & 0 & 0 & 0 & 0 & 0 & -1 & 2 \end{pmatrix} \quad (7)$$

We define the operators $\widehat{n}_T = (\widehat{n}_R - \widehat{n}_L)/2 + \text{constant}$ and $\widehat{\varphi}_T = (\widehat{\varphi}_R - \widehat{\varphi}_L)/2$ associated with the transmon dynamics. Introducing these operators, and noting that the total transmon charge $\widehat{n}_R + \widehat{n}_L$ is conserved, we can rewrite the Hamiltonian as

$$\begin{aligned} H &= \frac{E_{C,T}}{2} \widehat{n}_T^2 - E_{J,T}(\Phi_T) \cos(\widehat{\varphi}_T) + \frac{(2e)^2}{2} \sum_{j,l=1}^N \widehat{n}_j [\widehat{C}^{-1}]_{j,l} \widehat{n}_l + \\ &+ \frac{\varphi_0^2}{2L_J(\Phi_C)} \sum_{j=1}^N (\widehat{\varphi}_{j+1} - \widehat{\varphi}_j)^2 + \widehat{n}_T \sum_{j=1}^N \nu_j \widehat{n}_j \end{aligned} \quad (8)$$

where we defined $\widehat{\varphi}_{N+1} \equiv 0$. The transmon charging energy $E_{C,T}$ is given by

$$E_{C,T} = (2e)^2 \left\{ [\widehat{C}^{-1}]_{LL} + [\widehat{C}^{-1}]_{RR} - 2[\widehat{C}^{-1}]_{LR} \right\}. \quad (9)$$

The coupling of \widehat{n}_T to the charge on island j is given by

$$\nu_j = (2e)^2 \left\{ [\widehat{C}^{-1}]_{Rj} - [\widehat{C}^{-1}]_{Lj} \right\}. \quad (10)$$

Chain modes phase shift in the thermodynamic limit

In Fig. 4a we compare the measured relative frequency shift $\delta\phi_n(\Phi_T, \Phi_C)$ to the theoretically predicted transmon phase shift $\delta\phi(\omega, \Phi_T, \Phi_C)$ with which it is expected to agree in the thermodynamic limit. Here we provide the analytical formula for the phase shift $\phi(\omega, \Phi_T, \Phi_C)$ of a mode with frequency ω . (See Sec. G of the Supplementary Information for the derivation.) It reads

$$\tan \phi(\omega, \Phi_T, \Phi_C) = \frac{C_g - 2C_{\text{eff}}(\Phi_T, \omega)}{\sqrt{C_g(C_g + 4C_J)}} \frac{1}{\sqrt{\left(\frac{\omega_p(\Phi_C)}{\omega}\right)^2 - 1}}. \quad (11)$$

In this expression $\omega_p(\Phi_C) = 1/\sqrt{L_J(\Phi_C)(C_J + C_g/4)}$ is the plasma frequency of the chain, and

$$C_{\text{eff}}(\Phi_T, \omega) = C_1 - C_J - \frac{C_c^2}{C_0 - C_{\text{sh},T}} \frac{[(\hbar\omega)^2 C_0 - E_S(\Phi_T)]}{(C_0 + C_{\text{sh},T}) \frac{(\hbar\omega)^2}{(2e)^2} - 2E_S(\Phi_T)}. \quad (12)$$

has dimensions of capacitance. Finally, $E_S(\Phi_T)$ is an effective linear inductor energy associated with the Josephson junctions in the transmon, which nonetheless incorporates the transmon non-linearity, and is given by

$$E_S(\Phi_T) = E_{J,T}(\Phi_T) - \sqrt{E_{J,T}(\Phi_T)E_{C,T}/4}. \quad (13)$$

(See Sec. F of the Supplementary Material for further detail.) The theoretical $\delta\phi(\omega, \Phi_T, \Phi_C)$ curves plotted in panel a of Fig. 4 were obtained from $\phi(\omega, \Phi_T, \Phi_C)$ similarly to Eq. (2) as the difference

$$\delta\phi(\omega, \Phi_T, \Phi_C) = \phi(\omega, \Phi_T, \Phi_C) - \phi(\omega, \Phi_0/2, \Phi_C). \quad (14)$$

Analysis of the experimental data

To extract the relative frequency shift $\delta\phi_n(\Phi_T, \Phi_C)$ from the data presented in Fig. 2 of the main text, we go about as follows. At a fixed value of the magnetic field that determines Φ_T and Φ_C , we fit each of the peaks in the transmission spectrum individually with a Lorentzian. This gives the center frequency of the peaks. From these peak positions, we obtain $\delta\phi_n(\Phi_T, \Phi_C)$ experimentally using Eq. (1) at a particular Φ_T and Φ_C . Next we extract the transmon frequency ω_T for the transmon coupled to the chain from the experimentally determined $\delta\phi_n(\Phi_T, \Phi_C)$. The details are as follows. Empirically, we find that the experimentally determined $\delta\phi_n(\Phi_T, \Phi_C)$ vs. ω_n data-points fit an arctangent lineshape

$$F(\omega) = (1 - A) \left(\frac{1}{\pi} \arctan \left(\frac{2(\omega - \omega_T)}{\Gamma_T} \right) + \frac{1}{2} \right) + A \quad (15)$$

very well, for suitable choices of the parameters A , ω_T , and Γ_T . (In the parameter regime where our device operates, the theoretically predicted phase shift $\delta\phi(\omega, \Phi_T, \Phi_C)$ also closely approximates this line shape.) We therefore fit the measured $\delta\phi_n$ vs. ω_n at fixed Φ_T and Φ_C to Eq. (15), interpreting ω_T as the frequency and Γ_T as the resonance width of the transmon when it is coupled to the chain. Before we can quantitatively compare the experimental results for $\delta\phi_n(\Phi_T, \Phi_C)$ to the theoretically predicted $\delta\phi(\omega, \Phi_T, \Phi_C)$ (Eq. (11)), one final model parameter, namely the maximum transmon Josephson energy $E_{J,T,\text{max}}$ must be determined from the experimental data. The general procedure is as follows. Our theoretical model predicts that in the regime where the actual device operates, this transmon frequency is very nearly equal to the isolated ($L_J \rightarrow \infty$) transmon frequency, i.e. the chain only slightly renormalizes the transmon frequency, and indeed, we see little Φ_C dependence in the extracted ω_T . At $\Phi_T = n\Phi_0$, $n = 0, \pm 1, \pm 2, \dots$, where the transmon Josephson energy is maximal, we therefore use the isolated transmon result (see Sec. F of the Supplementary Information):

$$\omega_T(\Phi_T = n\Phi_0) = \sqrt{E_{C,T}E_{J,T,\text{max}}} - E_{C,T}/8 \quad (16)$$

Taking the average over n of the experimentally determined $\omega_T(\Phi_T = n\Phi_0)$, and using our first principle estimate for $E_{C,T}$ in Table I, we obtain

$$\omega_{T,\text{max}}/2\pi \equiv \omega_T(\Phi_T = 0)/2\pi = (4.64 \pm 0.01) \text{ GHz}, \quad (17)$$

$$E_{J,T,\text{max}}/h = (10.2 \pm 0.4) \text{ GHz} \quad (18)$$

The theoretical curves in Fig. 4a were then obtained using the system parameters in Table I in Eqs. (11), (14), (13), and (4). The full data set covers many transmon periods. Within a given transmon period, we generally analyze data at several values of Φ_T in the interval from $-0.3 \phi_0$ to $0.3 \phi_0$. Each transmon period is measured at different Φ_C . We also take into account the small variation in Φ_C as the transmon flux sweeps through one flux quantum. The experimental points in Fig. 4b are obtained as the transmon width Γ_T closest to $\Phi_T = 0$. The error bars come from the least square fit using Eq. (15). The theoretical width is obtained from a fit of the phase shift $\delta\phi(\omega, \Phi_T, \Phi_C)$ with the arctangent of Eq. (15).

Acknowledgements

The authors would like to thank F. Balestro, D. Dufeu, E. Eyraud, J. Jarreau, J. P. Girard, T. Meunier and W. Wernsdorfer, for early support with the experimental setup. Very fruitful discussions with C. K. Andersen, H. U. Baranger, D. Basko, S. Bera, J. J. Garcia Ripoll, S. M. Girvin, F. Hekking, K. Le Hur, C. Mueller, A. Parra and E. Solano are strongly acknowledged. The sample was fabricated in the clean rooms Nanofab and PTA (Upstream Technological Platform). This research was supported by the ANR under contracts CLOUD (project number

ANR-16-CE24-0005), GEARED (project number ANR-14-CE26-0018), by the UGA AGIR program, by the National Research Foundation of South Africa (Grant No. 90657), and by the PICS contract FERMICATS. J.P.M. acknowledges support from the Laboratoire d'excellence LANEF in Grenoble (ANR-10-LABX-51-01). R.D. and S.L. acknowledge support from the CFM foundation.

Author contributions

J.P.M., S.F. and N.R. designed the experiment. J.P.M. and N.R. fabricated the device. J.P.M. and S.L. performed the experiment and analysed the data with help from S.F, N.R. and I.S., while S.F.

and I.S. provided the theoretical support. All authors co-wrote the paper.

Competing interests

The authors declare that they have no competing financial interests.

Correspondence

Correspondence and requests for materials should be addressed to Nicolas Roch (email: nicolas.roch@neel.cnrs.fr).

- ¹ S. Haroche and J.-M. Raimond, Oxford University Press, Oxford, England (2006).
- ² N. M. Sundaresan, Y. Liu, D. Sadri, L. J. Szocs, D. L. Underwood, M. Malekakhlagh, H. E. Türeci, and A. A. Houck, *Physical Review X* **5**, 021035 (2015).
- ³ C. Wang, Y. Y. Gao, P. Reinhold, R. W. Heeres, N. Ofek, K. Chou, C. Axline, M. Reagor, J. Blumoff, K. M. Sliwa, L. Frunzio, S. M. Girvin, L. Jiang, M. Mirrahimi, M. H. Devoret, and R. J. Schoelkopf, *Science* **352**, 1087 (2016).
- ⁴ R. K. Naik, N. Leung, S. Chakram, P. Groszkowski, Y. Lu, N. Earnest, D. C. McKay, J. Koch, and D. I. Schuster, *Nature Communications* **8**, 1904 (2017).
- ⁵ Y. Liu and A. A. Houck, *Nature Physics* , 1 (2016).
- ⁶ P. Forn-Díaz, J. J. Garcia-Ripoll, B. Peropadre, J. L. Orgiazzi, M. A. Yurtalan, R. Belyansky, C. M. Wilson, and A. Lupaşcu, *Nature Physics* **13**, 39 (2017).
- ⁷ L. Magazzù, P. Forn-Díaz, R. Belyansky, J. L. Orgiazzi, M. A. Yurtalan, M. R. Otto, A. Lupaşcu, C. M. Wilson, and M. Grifoni, *Nature Communications* **9**, 1403 (2018).
- ⁸ M. Mirhosseini, E. Kim, V. S. Ferreira, M. Kalae, A. Sipahigil, A. J. Keller, and O. Painter, *arXiv.org* (2018), 1802.01708.
- ⁹ K. Le Hur, *Physical Review B* **85**, 140506 (2012).
- ¹⁰ M. Goldstein, M. H. Devoret, M. Houzet, and L. I. Glazman, *Physical Review Letters* **110**, 017002 (2013).
- ¹¹ B. Peropadre, D. Zueco, D. Porrás, and J. Garcia-Ripoll, *Physical Review Letters* **111**, 243602 (2013).
- ¹² N. Gheeraert, S. Bera, and S. Florens, *New Journal of Physics* **19**, 023036 (2017).
- ¹³ N. Gheeraert, X. H. H. Zhang, S. Bera, N. Roch, H. U. Baranger, and S. Florens, *arXiv.org* (2018), 1802.01665.
- ¹⁴ P. Jung, A. V. Ustinov, and S. M. Anlage, *Superconductor Science and Technology* **27**, 073001 (2014).
- ¹⁵ B. L. T. Plourde, H. Wang, F. Rouxinol, and M. D. LaHaye, in *SPIE Sensing Technology + Applications*, edited by E. Donkor, A. R. Pirich, and M. Hayduk (SPIE, 2015) p. 95000M.
- ¹⁶ G. Rastelli and I. M. Pop, *arXiv.org* (2017), 1712.07605v1.
- ¹⁷ T. Niemczyk, F. Deppe, H. Huebl, E. P. Menzel, F. Hocke, M. J. Schwarz, J. J. Garcia-Ripoll, D. Zueco, T. Hümmer, E. Solano, A. Marx, and R. Gross, *Nature Physics* **6**, 772 (2010).
- ¹⁸ F. Yoshihara, T. Fuse, S. Ashhab, K. Kakuyanagi, S. Saito, and K. Semba, *Nature Physics* **13**, 44 (2017).
- ¹⁹ S. J. Bosman, M. F. Gely, V. Singh, A. Bruno, D. Bothner, and G. A. Steele, *npj Quantum Information* **3**, 1 (2017).
- ²⁰ P. Forn-Díaz, L. Lamata, E. Rico, J. Kono, and E. Solano, *arXiv.org* (2018), 1804.09275.
- ²¹ A. Leggett, S. Chakravarty, A. Dorsey, M. Fisher, A. Garg, and W. Zwerger, *Reviews of Modern Physics* **59**, 1 (1987).
- ²² D. E. Logan, *Journal of Physics A: Mathematical and General* **38**, 1829 (2005).
- ²³ I. Bloch, J. Dalibard, and W. Zwerger, *Reviews of Modern Physics* **80**, 885 (2008).
- ²⁴ A. A. Houck, H. E. Türeci, and J. Koch, *Nature Physics* **8**, 292 (2012).
- ²⁵ I. Carusotto and C. Ciuti, *Reviews of Modern Physics* **85**, 299 (2013).
- ²⁶ K. Le Hur, L. Henriët, A. Petrescu, K. Plekhanov, G. Roux, and M. Schiró, *Comptes Rendus Physique* **17**, 808 (2016).
- ²⁷ A. C. Hewson, *The Kondo Problem to Heavy Fermions* (Cambridge, 1993).
- ²⁸ T. Weis, B. Küng, E. Dumur, A. K. Feofanov, I. Matei, C. Naud, O. Buisson, F. W. J. Hekking, and W. Guichard, *Physical Review B* **92**, 104508 (2015).
- ²⁹ M. H. Devoret, S. Girvin, and R. Schoelkopf, *Annalen der Physik* **16**, 767 (2007).
- ³⁰ J. Bourassa, J. M. Gambetta, A. A. A. Jr, O. Astafiev, Y. Nakamura, and A. Blais, *Physical Review A* **80**, 032109 (2009).
- ³¹ B. Peropadre, P. Forn-Díaz, E. Solano, and J. J. Garcia-Ripoll, *Physical Review Letters* **105**, 023601 (2010).
- ³² P. Forn-Díaz, J. Lisenfeld, D. Marcos, J. J. Garcia-Ripoll, E. Solano, C. J. P. M. Harmans, and J. E. Mooij, *Physical Review Letters* **105**, 237001 (2010).
- ³³ J. Braumüller, M. Marthaler, A. Schneider, A. Stehli, H. Rotzinger, M. Weides, and A. V. Ustinov, *arXiv.org* (2016), 1611.08404v1.
- ³⁴ N. K. Langford, R. Sagastizabal, M. Kounalakis, C. Dickel, A. Bruno, F. Luthi, D. J. Thoen, A. Endo, and L. DiCarlo, *Nature Communications* , 1 (2017).
- ³⁵ O. Astafiev, A. M. Zagorin, A. A. Abdumalikov, Y. A. Pashkin, T. Yamamoto, K. Inomata, Y. Nakamura, and J. S. Tsai, *Science* **327**, 840 (2010).
- ³⁶ I. C. Hoi, C. M. Wilson, G. Johansson, and T. Palomaki, *Physical Review Letters* **107**, 073601 (2011).
- ³⁷ M. Haerberlein, F. Deppe, A. Kurcz, J. Goetz, A. Baust, P. Eder, K. Fedorov, M. Fischer, E. P. Menzel, M. J. Schwarz, F. Wulschner, E. Xie, L. Zhong, E. Solano, A. Marx, J. J. Garcia-Ripoll, and R. Gross, *arXiv.org* (2015), 1506.09114v1.
- ³⁸ L. J. Geerligs, M. Peters, L. E. M. de Groot, A. Verbruggen, and J. E. Mooij, *Physical Review Letters* **63**, 326 (1989).
- ³⁹ E. Chow, P. Delsing, and D. B. Haviland, *Physical Review Letters* **81**, 204 (1998).
- ⁴⁰ R. Fazio, *Physics Reports* **355**, 235 (2001).

- ⁴¹ K. Cedergren, R. Ackroyd, S. Kafanov, N. Vogt, A. Shnirman, and T. Duty, *Physical Review Letters* **119**, 167701 (2017).
- ⁴² S. Corlevi, W. Guichard, F. Hekking, and D. Haviland, *Phys Rev Lett* **97**, 96802 (2006).
- ⁴³ I. M. Pop, I. Protopopov, F. Lecocq, Z. Peng, B. Panetier, O. Buisson, and W. Guichard, *Nature Physics* **6**, 589 (2010).
- ⁴⁴ A. Ergül, J. Lidmar, J. Johansson, Y. Azizoglu, D. Schaefer, and D. B. Haviland, *New Journal of Physics* **15**, 095014 (2013).
- ⁴⁵ K. K. Likharev and A. B. Zorin, *Journal of Low Temperature Physics* **59**, 347 (1985).
- ⁴⁶ J. E. Mooij and G. Schön, *Physical Review Letters* **55**, 114 (1985).
- ⁴⁷ N. Masluk, I. Pop, A. Kamal, Z. Mineev, and M. Devoret, *Physical Review Letters* **109**, 137002 (2012).
- ⁴⁸ M. Bell, I. Sadovskyy, L. Ioffe, A. Kitaev, and M. Gershenson, *Physical Review Letters* **109**, 137003 (2012).
- ⁴⁹ C. Altimiras, O. Parlavecchio, P. Joyez, D. Vion, P. Roche, D. Esteve, and F. Portier, *Applied Physics Letters* **103**, 212601 (2013).
- ⁵⁰ P. R. Muppalla, O. Gargiulo, S. I. Mirzaei, B. P. Venkatesh, M. L. Juan, L. Grünhaupt, I. M. Pop, and G. Kirchmair, *Phys Rev B* **97**, 024518 (2018).
- ⁵¹ P. Nataf and C. Ciuti, *Nature Communications* **1**, 72 (2010).
- ⁵² J. J. Garcia-Ripoll, B. Peropadre, and S. De Liberato, *Scientific Reports* **5**, srep16055 (2015).
- ⁵³ M. Malekakhlagh and H. E. Türeci, *Physical Review A* **93**, 012120 (2016).
- ⁵⁴ M. F. Gely, A. Parra-Rodriguez, D. Bothner, Y. M. Blanter, S. J. Bosman, E. Solano, and G. A. Steele, *Physical Review B* **95**, 245115 (2017).
- ⁵⁵ C. K. Andersen and A. Blais, *New Journal of Physics* **19**, 023022 (2017).
- ⁵⁶ E. Sánchez-Burillo, D. Zueco, J. J. Garcia-Ripoll, and L. Martín-Moreno, *Physical Review Letters* **113**, 263604 (2014).
- ⁵⁷ I. Snyman and S. Florens, *Physical Review B* **92**, 085131 (2015).
- ⁵⁸ C. Wang, C. Axline, Y. Y. Gao, T. Brecht, L. Frunzio, M. H. Devoret, and R. J. Schoelkopf, *arXiv.org* (2015), 1509.01854v1.
- ⁵⁹ O. Dial, D. T. McClure, S. Poletto, J. M. Gambetta, D. W. Abraham, J. M. Chow, and M. Steffen, *arXiv.org* (2015), 1509.03859v1.
- ⁶⁰ F. Lecocq, I. M. Pop, Z. Peng, I. Matei, T. Crozes, T. Fournier, C. Naud, W. Guichard, and O. Buisson, *Nanotechnology* **22**, 315302 (2011).
- ⁶¹ M. H. Devoret, *Les Houches Session LXIII* (1995).

Supplementary information for “A tunable Josephson platform to explore many-body quantum optics in waveguide”

A. Experimental setup

The full measurement setup is shown in Fig. S1. The device was placed in a dilution refrigerator at a base temperature of 20 mK, and the transmission measurements were performed using a Vector Network Analyzer (VNA). An additional microwave source was used for two-tone measurements, while a global magnetic field was applied via an external superconducting coil. Both the coil and the sample were held inside a mu-metal magnetic shield which is coated on the inside with a light absorber made out of epoxy loaded with silicon and carbon powder. The output line included two isolators at 20 mK, a HEMT amplifier at 4 K and a room temperature amplifier. The input line is attenuated at various stages, including a home-made filter that prevents stray-radiations from reaching the sample. We adopted a coaxial geometry with a dissipative dielectric (reference RS-4050 from resin systems company). The bandwidth of the measurement setup goes from 2.5 GHz to 13 GHz.

B. Chain dispersion relation

In this section we explain how we experimentally obtained the dispersion relation of the chain, and how we used it to determine the model parameters $L_{J,\min}$, C_g and C_J that characterize the chain. (See *Methods - Sample fabrication and parameters* in the main text.) The experimental data in Fig. S2a (reproduced from Fig. 2b in main text) was obtained by first tuning the external magnetic field to a point where $\Phi_T = \Phi_0/2$ so that $E_{J,T}(\Phi_T) = 0$. (Green dashed line in the inset to Fig. S2a.) This leads to vanishingly low transmon frequency. As a result, the transmon does not contribute any degrees of freedom that can hybridize with the bare modes of the chain. In order to realize a good fit, one needs to measure the spectrum in a wide frequency band (0.1 GHz to 20 GHz). One is however limited by the bandwidth of the setup (2.5 GHz to 13 GHz). This difficulty can be overcome by performing a two-tone measurement¹⁻³, taking advantage of the fact that the array is not perfectly linear. As a consequence, when applying a microwave tone at a given resonance of the chain, the other resonant frequencies are shifted by the cross Kerr effect. With the Vector Network Analyzer (VNA), we proceed by measuring the transmission of the system at a fixed frequency $\omega_{\text{VNA}} = \omega_1$ where ω_1 matches a given resonance frequency of the circuit. Then with a microwave source

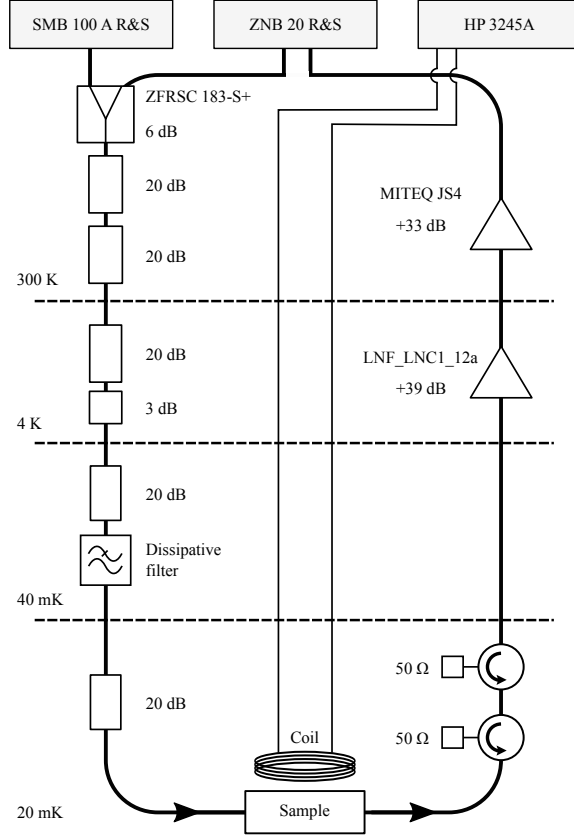


FIG. S1. **Experimental setup.**

we apply a second tone at a variable frequency ω_{MW} . Whenever ω_{MW} equals any other resonance frequency of the circuit, ω_1 shifts to $\tilde{\omega}_1$ due to the cross Kerr effect, so that $\omega_{\text{VNA}} \neq \tilde{\omega}_1$, which leads to a dip in transmission. The value of ω_{MW} at these dips provides all the resonances of the system. Because we measure at a constant frequency ω_{VNA} inside the setup bandwidth, we are not limited by the frequency range of our measurement setup anymore. A typical two-tone measurement is shown in Fig. S2b, where we fit each dip separately with a Lorentzian. The center frequencies obtained from these fits are the experimental points in Fig. S2a for the eigenmodes of the chain.

In order to fit the experimental data for the chain modes, we assume that the left end of the chain is open when $\Phi_{\text{T}} = 0.5 \Phi_0$ ($E_{\text{J,T}} = 0$). We also take the right end of the chain to be grounded. Given that the chain SQUIDS are designed to have a Josephson energy several thousand times their charging energy ($E_{\text{J}}/E_{\text{C}} = 8400$), we can model the Josephson junctions in the chain as linear inductors with inductance $L_{\text{J}}(\Phi_{\text{C}}) = \varphi_0^2/E_{\text{J}}(\Phi_{\text{C}})$, with $\varphi_0 = \hbar/2e$ the reduced flux quantum. The theoretical dispersion relation can be obtained applying Kirchoff's laws to one chain cell of length a . (See the circuit diagram in Fig. 1a in the main text.) Denoting the flux at node j as Φ_j , we obtain

$$\frac{1}{L_{\text{J}}(\Phi_{\text{C}})} (\Phi_{j-1} - \Phi_j) + C_{\text{J}} (\ddot{\Phi}_{j-1} - \ddot{\Phi}_j) - \frac{1}{L_{\text{J}}(\Phi_{\text{C}})} (\Phi_j - \Phi_{j+1}) - C_{\text{J}} (\ddot{\Phi}_j - \ddot{\Phi}_{j+1}) - C_{\text{g}} \ddot{\Phi}_j = 0. \quad (\text{S1})$$

Now if we use as ansatz a plane waves $\Phi_j = A \exp i(\omega t - \kappa j a) + B \exp i(-\omega t + \kappa j a)$ and solve for ω we obtain the dispersion relation for a bare chain

$$\omega(\kappa) = \frac{1}{\sqrt{L_{\text{J}}(\Phi_{\text{C}}) C_{\text{J}}}} \sqrt{\frac{1 - \cos(\kappa a)}{1 - \cos(\kappa a) + \frac{C_{\text{g}}}{2C_{\text{J}}}}}. \quad (\text{S2})$$

The boundary conditions at site 0 (vacuum) and at site N (grounded) read

$$\left. \frac{\partial \Phi_j}{\partial(ja)} \right|_{j=0} = 0, \quad (\text{S3})$$

$$\dot{\Phi}(N) = 0, \quad (\text{S4})$$

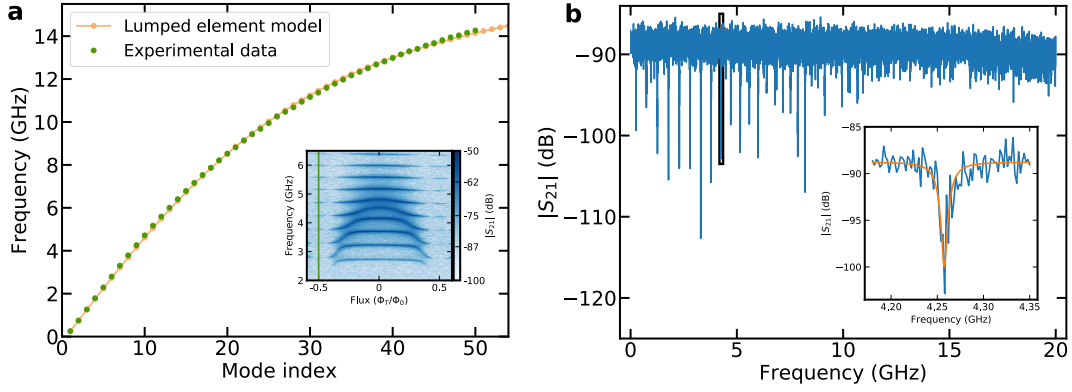


FIG. S2. **Extraction of the individual chain modes.** **a** Dispersion relation of the chain, reproduced from Fig. 2b in main text. The inset shows a colourscale plot of the transmission amplitude as function of Φ_T and probe frequency, with a green line indicating the fixed flux value employed to determine the dispersion relation of the uncoupled chain. **b** Two tone measurement of the modes of the array. The frequency trace is along the green line in panel *a*. The inset shows a lorentzian fit of one of the dips. The measurement was taken with $P_{VNA} = -10$ dBm and $P_{MW} = 10$ dBm at room temperature. The frequency of the VNA was set to $\omega_{VNA} = 5.1692$ GHz.

which restricts the values of κa to

$$\kappa a = \frac{\left(n - \frac{1}{2}\right) \pi}{N} \quad n = 1, 2, \dots, N. \quad (\text{S5})$$

Since the areas of chain SQUID loops are much smaller than that of the transmon SQUID loop, at $\Phi_T = \Phi_0/2$ we can tune the flux Φ_C through each chain SQUID to a multiple of Φ_0 , so that the chain SQUID inductance is minimal, i.e. $L_J(\Phi_C) = L_{J,\min}$, without appreciably changing the transmon flux Φ_T from its value $\Phi_0/2$. (See Eq. (3) in the *Methods* section of the main text.) Using Eq. (S2) with the κ values from Eq. (S5), we fit the experimental data in Fig. S2a (orange curve), thus fixing the minimal Josephson inductance $L_{J,\min}$ and the capacitance to ground C_g . We obtain the Josephson self-capacitance C_J using the empirical formula⁴

$$C_J = 45 \text{ fF}/\mu\text{m}^2 \times \text{junction area}. \quad (\text{S6})$$

The error for C_J is just the error we obtain for the measurement of the Josephson junction's area using a Scanning Electron Microscope. The error for $L_{J,\min}$ and C_g are the values where the deviation between the experiment and the fit was below 5%.

C. Additional phase shift data

In this section we present a further selection of relative phase shift data $\delta\phi_n$ obtained for various (Φ_T, Φ_C) combination. This is only a small subset of the full data set, and the agreement between theory and experiment exhibited here is representative of the full data set. Results presented here complement Fig. 4a of the main text. The parameters used to obtain the theory curves are the ones of Table S1.

D. Transmon qubit capacitances estimation

In order to obtain the capacitances listed in Table S1 (reproduced from the main text) we use EM simulation software (Sonnet). This software solves Maxwell's equations in three dimensions for the specified design of our device and gives the scattering parameters of the system as a function of frequency. We simulate two parts of the design independently, the interdigital capacitors and the SQUID of the transmon qubit.

1. Interdigital capacitors

Since we are only interested in modelling the capacitors of the transmon, we remove the chain from the simulation and replace the Josephson junction of the transmon by a linear inductor, L_{test} . We place two ports at both ends of

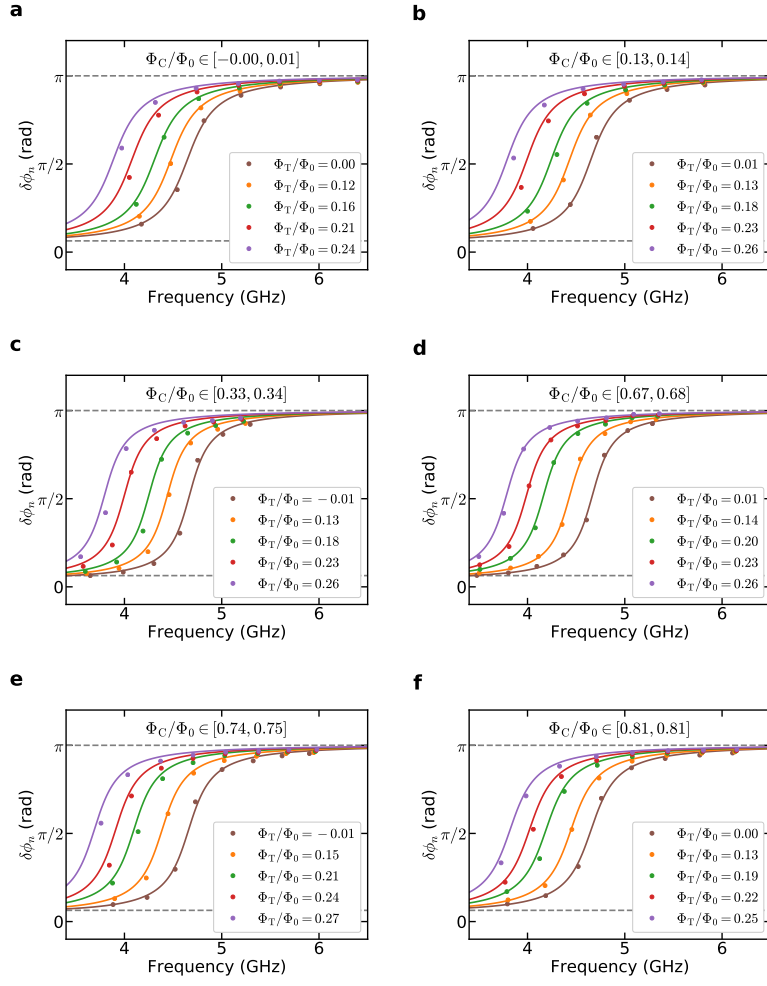


FIG. S3. **Consistency of the theoretical model for several transmon and chain fluxes.** The various panels show the relative phase shift $\delta\phi_n$ of the discrete chain modes as a function of mode frequency ω_n for different transmon fluxes Φ_T and chain fluxes Φ_C . The solid lines are fits using Eq. (14) of the main text with the parameters of the circuit kept fixed.

Chain parameters		Transmon qubit parameters	
$L_{J,\min}$	(0.33 ± 0.02) nH	$C_{g,T2}$	(33 ± 1) fF
C_g^g	(0.13 ± 0.01) fF	$C_{g,T}$	(48 ± 2) fF
C_J	(259 ± 14) fF	C_c	(119 ± 2) fF
N	4700	C_{sh}	(6.9 ± 0.1) fF
d (asymmetry)	0.25	$C_{J,T}$	(5.2 ± 0.3) fF
		$E_{J,T,\max}/h$	(10.2 ± 0.4) GHz
		$E_{C,T}/h$	(2.4 ± 0.1) GHz

TABLE S1. **Sample parameters.**

the design, and set the characteristic impedance of the port on the left to Z_{left} and for the port on the right to Z_{right} .

From the EM simulation we obtain the transmission of the system, S_{21} , as a function of frequency. We fit the prediction of the linear model of the qubit to this. This model consists of the capacitance network shown in Fig. S4 in red. The transmission of this system is given by Eq. (S7)⁵ where A , B , C and D are the ABCD matrix elements⁶ for the capacitance network plus the linear inductor.

$$S_{21} = \frac{2\sqrt{Z_{\text{left}}Z_{\text{right}}}}{AZ_{\text{right}} + B + CZ_{\text{left}}Z_{\text{right}} + DZ_{\text{left}}}. \quad (\text{S7})$$

In theory L_{test} , Z_{left} , Z_{right} do not affect the obtained capacitances and can be chosen arbitrarily. However, due to the fact that the lumped element model is an idealization, we observed a small shift of the capacitances as a function of L_{test} . (This shift was not observed as a function of Z_{left} or Z_{right}). To minimize the effect of this shift, we set

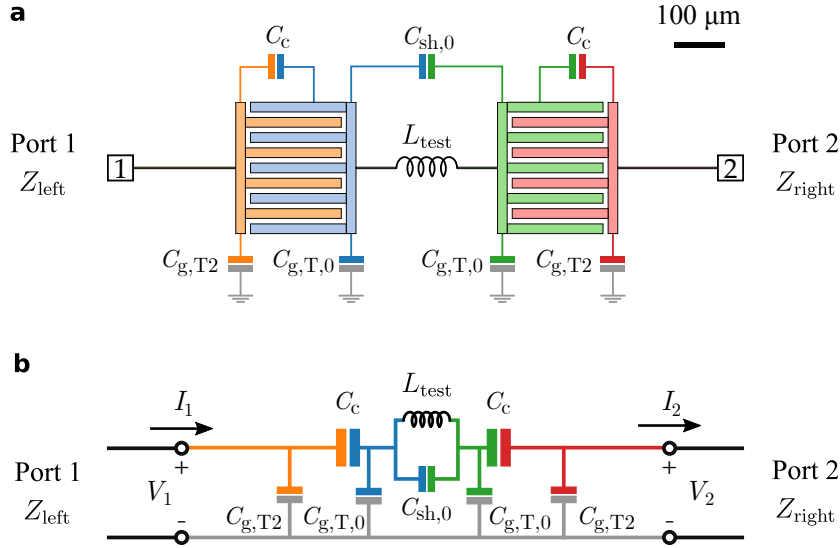


FIG. S4. **Model for the linear transmon coupling.** **a** Real capacitor design. **b** Lumped element model used in the EM simulations.

$L_{\text{test}} = 22 \text{ nH}$ which gives a resonance frequency close to ω_T .

We perform two simulations. In the first one we set $Z_{\text{left}} = Z_{\text{right}} = 50 \Omega$. Due to the low impedance of the ports, we can neglect $C_{g,T2}$ and we therefore fit only C_c , $C_{g,T,0}$ and $C_{sh,0}$. Then we perform a second simulation with $Z_{\text{left}} = 50 \Omega$ and $Z_{\text{right}} = 3000 \Omega$. Now we fit only $C_{g,T2}$ keeping the other capacitances constant. In this way we obtain all the capacitances in Fig. S4 independently. Note that the self-capacitance of the junction $C_{J,T}$ cannot be simulated and is therefore obtained from Eq. (S6). The errors are obtained as the maximum range where the difference between simulation and model is smaller than 10%. The two fits are shown in Fig. S5.

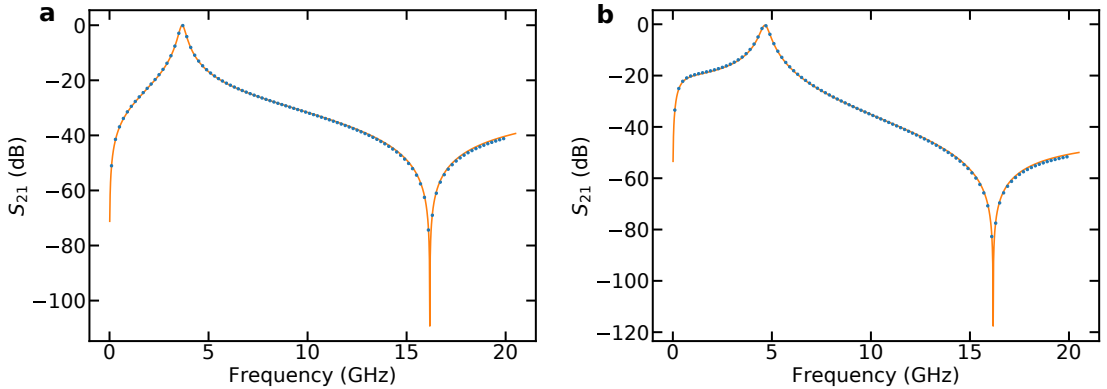


FIG. S5. **Extraction of the coupling capacitances.** Fit of the obtained S_{21} parameter to a linear model with $Z_{\text{right}} = 50 \Omega$ (left panel **a**) and $Z_{\text{right}} = 3000 \Omega$ (right panel **b**).

2. Stray capacitances from the transmon SQUID

The transmon qubit has a SQUID with a large loop ($\sim 55 \mu\text{m} \times 1.2 \mu\text{m}$). Due to its large size, the capacitances associated to this SQUID are not negligible. In Fig. S6a the SQUID design with the different capacitances is given. The lumped element model used for simulating the system is shown in Fig. S6b.

We follow the same procedure as before. Given the small number of fitting parameters ($C_{sh,S}$ and $C_{g,S}$) we can perform a single fit with $Z_{\text{left}} = 50 \Omega$ and $Z_{\text{right}} = 3000 \Omega$. The result of the fit is shown in Fig. S7 with the obtained

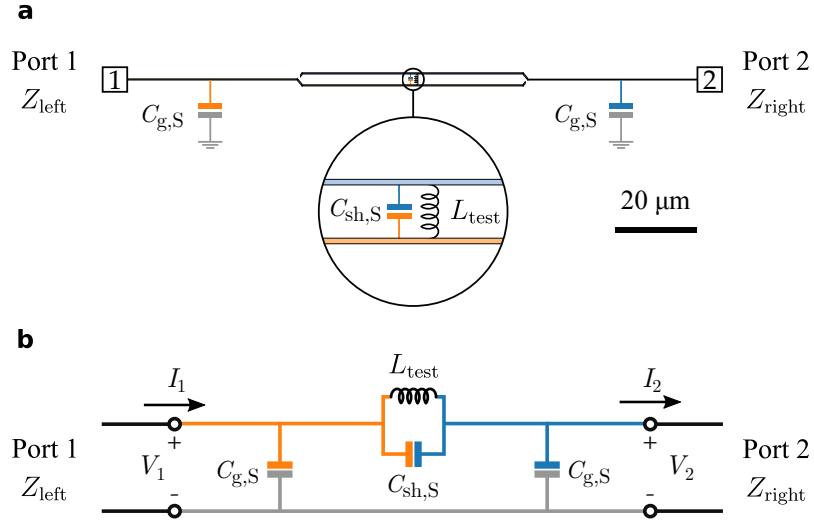


FIG. S6. **Internal capacitance model for the transmon.** **a** Real design of the SQUID of the transmon qubit. In the inset the shunting capacitance $C_{\text{sh},S}$ and test inductance L_{test} are shown. **b** Lumped element model used to simulate the capacitances of the system.

capacitance values. The SQUID increases both the shunting capacitance and the ground capacitance of the transmon

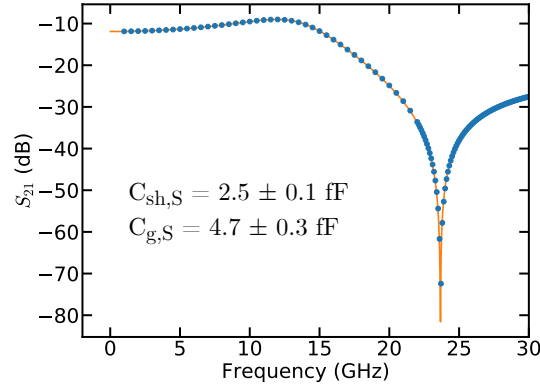


FIG. S7. **Extraction of the internal capacitances.** SQUID capacitances estimation. Simulated transmission (blue circles) and fit from the lumped element model, orange solid line. The simulation was performed setting $Z_{\text{left}} = 50 \Omega$ and $Z_{\text{right}} = 3000 \Omega$.

qubit.

E. How does the transmon decay rate depends on the impedance of the environment?

Before quantitatively modeling the system, in this section we try to gain a qualitative understanding of how the transmon decay rate Γ_T depends on the characteristic impedance of the chain. Since we are only aiming for a qualitative description, we treat the transmon SQUID loop as an LC circuit, ignoring its non-linearity. We retain the capacitive couplings C_c , that couple the transmon to the chain and the 50Ω transmission line. We drop the ground capacitances $C_{g,T}$ and $C_{g,T2}$ that shunt the chain at high frequencies, thus idealizing to the situation where the chain produces an optimal broadening of the transmon resonance. We consider an infinite chain. Since we are not interested here in modeling frequency dependent transport through the system, but only in the effect the chain has on the transmon, we replace the complicated frequency dependent impedance of the chain $Z_{\text{chain}}(\omega)$ with its constant characteristic impedance $R = \sqrt{L_J/C_g}$. We replace the 50Ω (low impedance) transmission lines by ground connections. These assumptions produce the simple linear circuit depicted in Fig. S8.

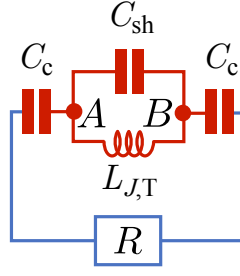


FIG. S8. **Toy model of the whole circuit.** Simplified lumped element model used to qualitatively understand the link between the transmon decay rate and the impedance of the environment.

Within this linear model, the resonance frequency ω_T and decay rate Γ_T of the transmon are obtained as respectively the real and imaginary parts of the relevant pole of the frequency dependent impedance between A and B in the circuit diagram. This impedance is given by

$$Z_{AB}(\omega) = \frac{iL_{J,T}\omega(2 + iC_cR\omega)}{(2 + iRC_c\omega)(1 - L_{J,T}C_{sh}\omega^2) - L_{J,T}C_c\omega^2} \quad (\text{S8})$$

We have to note here that we have oversimplified the model, which now predicts an overdamped regime at small C_{sh} . In the real device, overdamping is prevented by the sizable capacitances $C_{g,T}$ and $C_{g,T2}$, which we have dropped. A quick fix, is to use a value for C_{sh} that is comparable to $C_{g,T}$ and $C_{g,T2}$ (several tens of fF), rather than its actual value of 4.4 fF. The behavior of the resonance frequency is easy to understand. At small R , one effectively has an LC circuit with capacitance $C_{sh} + C_c/2$ and resonance frequency $\omega_T = 1/\sqrt{L_{J,T}(C_{sh} + C_c/2)}$, while at large R , one has an isolated SQUID loop with resonance frequency $\omega_T = 1/\sqrt{L_{J,T}C_{sh}}$.

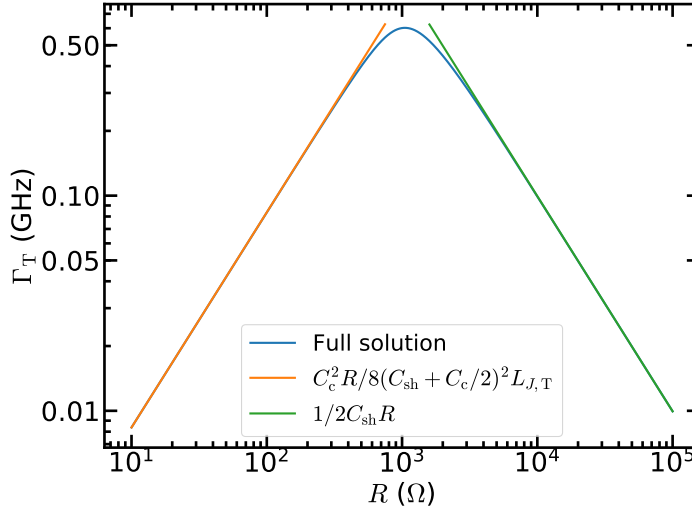


FIG. S9. **Bath engineered dissipation from the toy model.** Evolution of the transmon decay rate Γ_T versus the value of the resistance R , as described in the simplified circuit of Fig. S8.

In Fig. S9 we present the behavior of Γ_T vs. R for $C_c = 119$ fF (its actual value) and $C_{sh} = 80$ fF, chosen to give rough quantitative agreement with the experimental results we present in the Fig. 4 of the main text, although the qualitative behavior does not change if we change C_{sh} moderately. At small R , the behavior of the decay rate Γ_T is

$$\Gamma_T = \frac{C_c^2 R}{8(C_{sh} + C_c/2)^2 L_{J,T}} \quad (\text{S9})$$

(proportional to R) while at large R , it is given by

$$\Gamma_{\text{T}} = \frac{1}{2C_{\text{sh}}R} \quad (\text{S10})$$

(proportional to $1/R$). A good estimate of the value R_* that maximizes Γ_{T} is obtained by equating the small and large R asymptotic expressions for Γ_{T} . This yields

$$R_* = \left(1 + \frac{2C_{\text{sh}}}{C_{\text{c}}}\right) Z_{\text{T,simp}} \quad (\text{S11})$$

where $Z_{\text{T,simp}} = \sqrt{L_{\text{J,T}}/C_{\text{sh}}}$ is the characteristic impedance of the transmon, in the simplified circuit of Fig. S8. Thus the largest coupling (as measured by Γ_{T}) is obtained when the characteristic impedances of the transmon and chain match up to factors of order one, a result that is familiar in microwave engineering. At this optimal chain impedance, the decay rate Γ_{T} is proportional to ω_{T} with a proportionality constant that is a function of $C_{\text{c}}/C_{\text{sh}}$. This constant can reach values of order one, implying ultra-strong coupling is attainable. In our actual device, we find Γ_{T} to be a decreasing function of L_{J} , in the L_{J} window to which we have access, suggesting that the lowest chain impedance that we can reach, is larger than the optimal value R_* . When we compare the characteristic impedances $Z_{\text{T}} = \hbar/(2e)^2 \sqrt{2E_{\text{C,T}}/E_{\text{J,T}}} \simeq 760 \Omega$ (transmon) and $Z_{\text{C}} = \sqrt{L_{\text{J}}/C_{\text{g}}} \simeq 1590 \Omega$ (chain) of the actual device, we see that indeed $Z_{\text{C}} > Z_{\text{T}}$. Note that here we took a realistic estimate for the transmon impedance, that includes the effect of the capacitances $C_{\text{g,T}}$ and $C_{\text{g,T2}}$ which were dropped in our qualitative model. Had we naively taken $Z_{\text{T}} = \sqrt{L_{\text{J,T}}/C_{\text{sh}}}$ we would have obtained $Z_{\text{T}} = 1990 \Omega$, which though still close to the chain impedance, might have lead us to expect to observe a maximal value for Γ_{T} as we sweep the L_{J} window to which we have access.

F. Dealing with the transmon nonlinearity

The results in Fig. 3 in the main text confirm that the transmon qubit is a non-linear quantum circuit element that is strongly coupled to the chain. Here we review a standard way to deal with this anharmonicity.⁷ The method is known as the self-consistent harmonic approximation (SCHA) because the anharmonic term is replaced by a harmonic one whose magnitude is determined self-consistently, via the variational principle. We also determine the regime of validity of the approximations we introduce. Let us consider the complete Hamiltonian of the device, neglecting only the weak non-linearity in the chain elements:

$$H = \frac{E_{\text{C,T}}}{2} \hat{n}_{\text{T}}^2 - E_{\text{J,T}} \cos(\hat{\varphi}_{\text{T}}) + \frac{(2e)^2}{2} \sum_{j,l=1}^N \hat{n}_j \left[\hat{C}^{-1} \right]_{j,l} \hat{n}_l + \frac{E_{\text{J}}}{2} \sum_{j=1}^N (\hat{\varphi}_{j+1} - \hat{\varphi}_j)^2 + \hat{n}_{\text{T}} \sum_{j=1}^N \nu_j \hat{n}_j. \quad (\text{S12})$$

Here we found it convenient to define an operator $\hat{\varphi}_{N+1} \equiv 0$ which is not an extra degree of freedom, but simply the zero operator. To shorten notation we don't indicate the Φ_{T} dependence of $E_{\text{J,T}}$ or the Φ_{C} dependence of E_{J} explicitly here. Were it not for the term $-E_{\text{J,T}} \cos(\hat{\varphi}_{\text{T}})$, the quantum system described by the Hamiltonian in Eq. (S12) (Eq. 8 in the main text) would have been equivalent to a set of coupled harmonic oscillators, and therefore straightforward to solve. The term $-E_{\text{J,T}} \cos(\hat{\varphi}_{\text{T}})$, not being quadratic in $\hat{\varphi}_{\text{T}}$, produces an interacting many-body problem. The strategy will be to replace the transmon terms in H with more tractable, yet accurate counterparts. For this purpose our starting point is to consider the Hamiltonian H in the limit where the inductances L_{J} between chain nodes go to infinity ($E_{\text{J}} \rightarrow 0$), so that the charge on each chain island is conserved, and we can treat \hat{n}_j , $j \in \{1; \dots; N\}$ as ordinary numbers. Since the transmon then does not couple to any dynamical degrees of freedom, we refer it as isolated. The conserved chain charges contribute to the offset charge for \hat{n}_{T} . We will abuse notation slightly and still denote the transmon's charge degree of freedom, which now incorporates this additional offset, by \hat{n}_{T} . The isolated transmon Hamiltonian, in which reference to the conserved charges \hat{n}_{α} , $\alpha \in \{1; \dots; N\}$ has been eliminated, reads

$$H_{\text{T}} = \frac{E_{\text{C,T}}}{2} \hat{n}_{\text{T}}^2 + E_{\text{J,T}} [1 - \cos(\hat{\varphi}_{\text{T}})]. \quad (\text{S13})$$

Due to charge being quantized in units of $2e$, the state space of H_{T} is restricted to states $|\psi\rangle$ for which

$$e^{i2\pi \hat{n}_{\text{T}}} |\psi\rangle = e^{-i2\pi n_{\text{T}}} |\psi\rangle, \quad (\text{S14})$$

where the offset charge n_{T} (an ordinary number) contains contributions from the total transmon charge, the charge on each chain island, and from gate charges. We denote the eigenbasis of \hat{n}_{T} by $|\nu\rangle$, i.e.

$$\hat{n}_{\text{T}} |\nu\rangle = \nu |\nu\rangle. \quad (\text{S15})$$

Owing to (S14), ν is quantized such that

$$\nu + n_T \in \mathbb{Z}. \quad (\text{S16})$$

The matrix elements of H_T in the $|\nu\rangle$ basis read

$$\langle \nu | H_T | \nu' \rangle = \frac{E_{C,T} \nu^2}{2} \delta_{\nu,\nu'} + \frac{E_{J,T}}{2} (\delta_{\nu,\nu'+1} + \delta_{\nu,\nu'-1}). \quad (\text{S17})$$

The problem is equivalent to that of a charge e particle of mass $E_{C,T}^{-1}$ confined to a ring of circumference 2π that

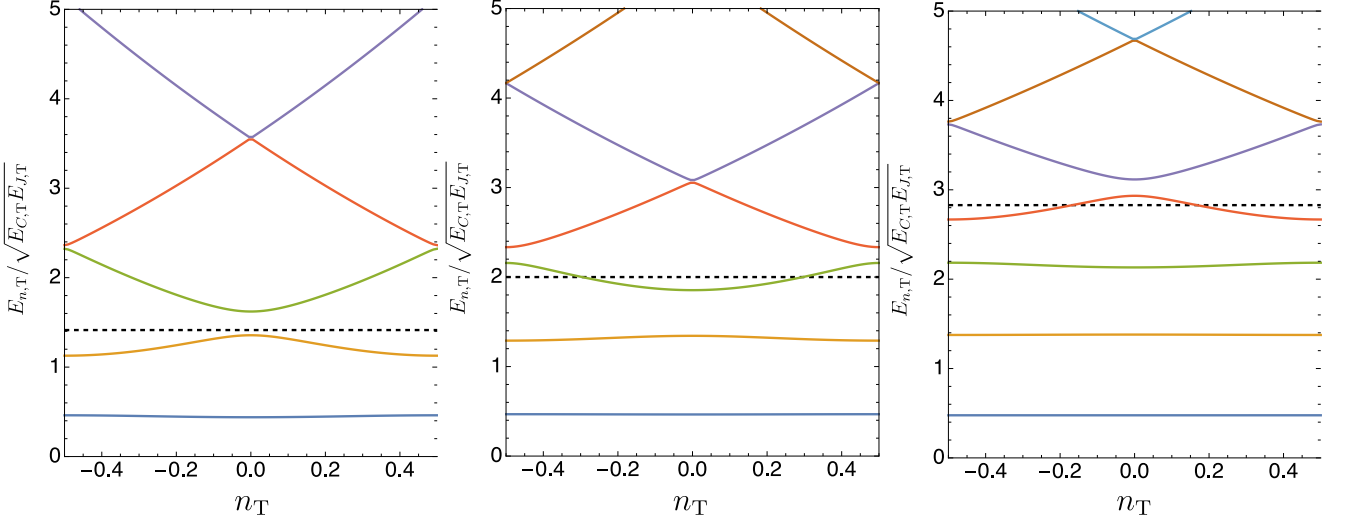


FIG. S10. **Isolated transmon spectrum as a function on the offset charge n_T .** Left panel: $E_{J,T}/E_{C,T} = 1/2$. Middle panel: $E_{J,T}/E_{C,T} = 1$. Right panel: $E_{J,T}/E_{C,T} = 2$. In each case a dashed line indicates the energy $2E_{J,T}$, maximum potential energy.

is threaded by a flux of n_T times the flux quantum $\Phi_0 = h/2e$. The phase observable $\hat{\varphi}_T$ plays the role of the position coordinate, and the particle has an electrostatic potential energy $E_{J,T}(1 - \cos \hat{\varphi}_T)$. This system is easily solved numerically. In Figure S10 the low energy spectrum is plotted as a function of the offset charge n_T , for three $E_{C,T}/E_{J,T}$ ratios. States with energies sufficiently less than the height $2E_{J,T}$ of the cosine well are insensitive to the offset charge n_T . This is easy to understand in the equivalent picture of the particle confined to a ring: Sensitivity to the flux inside the ring requires the interference of paths with different winding numbers around the ring. However, at energies below $2E_{J,T}$, paths with non-zero winding number are exponentially suppressed by the tunneling amplitude to go through the cosine barrier. States with energy $\gtrsim 2E_{J,T}$ on the other hand are sensitive to the offset charge n_T . As n_T varies from 0 to $1/2$ (half a Cooper pair), each of these energies sweep through an interval (or band) of width comparable to the spacing between levels. In the equivalent picture of a particle on a ring, this is a manifestation of the Aharonov Bohm effect. In a real experiment, the offset charge n_T is subject to environmental noise. Performing spectroscopy on the levels sensitive to n_T will therefore produce a noisy signal in which the extracted level energy “jumps around” inside the band through which the energy sweeps as n_T is varied.

When we reduce L_J from infinity to its actual value, thus coupling the transmon to dynamical degrees of freedom in the chain, a numerically exact solution is no longer possible, given the large size of the Hilbert space. An obvious approximation scheme for states with energies below $2E_{J,T}$ is the following. For these states, the phase observable $\hat{\varphi}_T$ is unlikely to make excursions over the top of the cosine barrier (phase slips) at $\varphi_T = \pm\pi$. For such states it should therefore be permissible to replace the ring to which the particle is confined with the whole real line, and the cosine potential with a parabola. Note that this approximation ignores the restriction (S14), responsible for charge quantization. For states with energies $\ll E_{J,T}$, the phase is confined very close to the minimum at $\varphi = 0$ of the cosine potential, and the replacement $E_{J,T}(1 - \cos \hat{\varphi}_0) \rightarrow E_{J,T} \hat{\varphi}_0^2/2$ is legitimate. This leads to a harmonic spectrum $\omega_n = \sqrt{E_{C,T} E_{J,T}}(n+1/2)$. However, the quadratic approximation can be improved to have a larger regime of validity, in the following way. We approximate the eigenstates of the **isolated** transmon as those of the parent Hamiltonian

$$H_P = \frac{E_{C,T}}{2} \hat{n}_T^2 + \frac{E_S}{2} \hat{\varphi}_T^2, \quad (\text{S18})$$

where the parameter E_S is optimized according to some criterium in order to give the best possible agreement with the exact solution. Here we use the criterion that the energy E_S should be chosen to minimize $\langle H_T \rangle$ where the expectation value is taken with respect to the ground state of H_P . For given E_S , the eigenstates and energies of H_P are

$$|n\rangle = \frac{(B^\dagger)^n}{\sqrt{n!}} |0\rangle, \quad E_n^{(0)} = \omega_T(n + 1/2), \quad n = 0, 1, 2, \dots, \quad \omega_T = \sqrt{E_{C,T}E_S}, \quad (\text{S19})$$

where

$$B|0\rangle = 0, \quad B = \lambda \hat{n}_T + i \hat{\varphi}_T / 2\lambda, \quad \lambda = \frac{1}{\sqrt{2}} \left(\frac{E_{C,T}}{E_S} \right)^{1/4}. \quad (\text{S20})$$

Expressed in terms of the bosonic operators B and B^\dagger , and manipulated into normal ordered form, the full transmon Hamiltonian reads

$$H_T = \omega_T \left[B^\dagger B + \frac{1}{2} \right] + E_{J,T} \left\{ 1 - \frac{e^{-\lambda^2/2}}{2} \left[e^{\lambda B^\dagger} e^{-\lambda B} + e^{-\lambda B^\dagger} e^{\lambda B} \right] \right\} + \frac{E_S}{2} \lambda^2 [(B^\dagger)^2 + B^2 - 2(B^\dagger B + 1)]. \quad (\text{S21})$$

The expectation value $\langle 0|H_T|0\rangle$ evaluates to

$$\langle 0|H_T|0\rangle = \frac{\omega_T}{4} + E_{J,T} \left(1 - e^{-\lambda^2/2} \right) = \frac{\sqrt{E_{C,T}E_S}}{4} + E_{J,T} \left[1 - e^{-\sqrt{E_{C,T}E_S}/4} \right]. \quad (\text{S22})$$

The minimal value for $\langle 0|H_T|0\rangle$ is produced by E_S satisfying the equation

$$E_S = E_{J,T} e^{-\sqrt{E_{C,T}E_S}/4}, \quad (\text{S23})$$

which can also be written as an equation

$$\omega_T = \sqrt{E_{J,T}E_{C,T}} e^{-E_{C,T}/8\omega_T}, \quad (\text{S24})$$

determining the transmon frequency ω_T . We note that in principle, the approximation can be further improved by treating H_P with the optimized value (S23) for E_S as the zero'th order approximation and treating $H_T - H_P$ as a small perturbation. In general, the leading corrections in such a perturbation expansion are of first order in λ^2 . However, for the ground and first excited states, it is one order higher, i.e. λ^4 . Thus, the approximation $H_T \simeq H_P$ is particularly accurate for the ground and first excited states of the transmon, which given the probe power and plasma frequency of the chain, are the ones we are interested in, in the experiment. The assumed smallness of λ allows us to solve approximately the self-consistency equation (S23) to get

$$E_S = E_{J,T} - \frac{1}{4} \sqrt{E_{C,T}E_{J,T}} + \mathcal{O}(E_{C,T}), \quad (\text{S25})$$

which gives an excitation energy

$$\omega_T = \sqrt{E_{C,T}E_{J,T}} - E_{C,T}/8 + \mathcal{O}\left(\frac{E_{C,T}^2}{\sqrt{E_{C,T}E_{J,T}}}\right). \quad (\text{S26})$$

In Figure S11 we compare the results (S24) and (S26) to the exact excitation energy of the isolated transmon, and find that in the regime where sensitivity to the offset charge n_T is weak, i.e. $E_{J,T}/E_{C,T} \gtrsim 1$, the approximation (S26) is indistinguishable from the more sophisticated (S24). Now we turn to the case $E_J > 0$ where the transmon is coupled to the dynamical degrees of freedom in the chain. We take the same approach as before. In principle, it is possible to generalize the previous calculation in the following way. When $E_J > 0$, we may choose E_S so that it minimizes $\langle 0|H|0\rangle$, where H is the full Hamiltonian in (Eq. 4 in the main text)

$$H = \frac{(2e)^2}{2} \tilde{n}^T \hat{C}^{-1} \tilde{n} - \frac{1}{2} \tilde{\varphi}^T \hat{J} \tilde{\varphi} - E_{J,T} \cos(\hat{\varphi}_R - \hat{\varphi}_L), \quad (\text{S27})$$

and $|0\rangle$ is the ground state of the parent Hamiltonian that is obtained from H by making the replacement $E_{J,T}(1 - \cos \hat{\varphi}_T) \rightarrow E_S \hat{\varphi}_T^2/2$. We have implemented this approach, but find that it yields an insignificant improvement upon the simpler approach of simply taking $E_S = E_{J,T} - \sqrt{E_{J,T}E_{C,T}}/4$, at least in the one photon sector, and for the parameters of the current device.

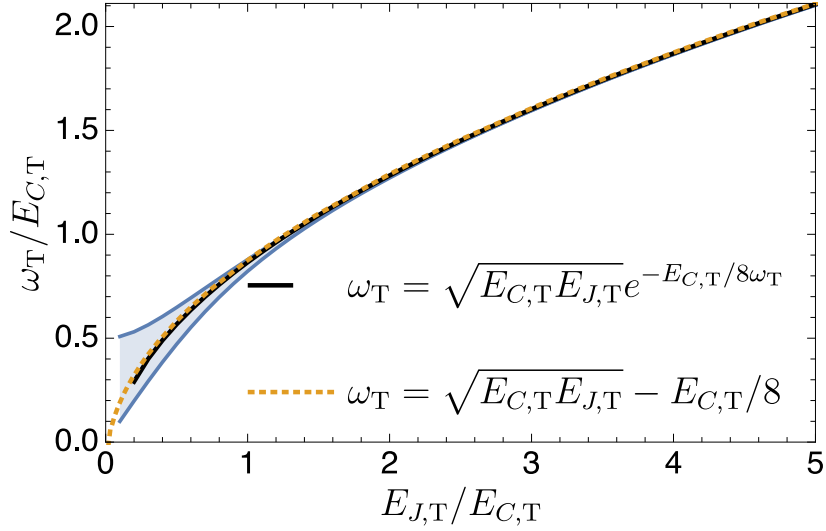


FIG. S11. **From the transmon to the Cooper pair box.** Excitation energy ω_T from the ground state to the first excited state of the isolated transmon. The shaded area represents the range of values obtained for the exact result when the offset charge n_T is swept through $[0, 1/2]$. The solid black line represents the fully self-consistent result (S24) while the dashed line represents the simple approximation (S26).

G. Analytical formula for the Scattering Phase Shift

In the section *Methods - Analytical formula for the Scattering Phase Shift* we presented a formula (Eq. 11) for the phase shift $\phi(\omega, \Phi_T, \Phi_C)$ of a mode with frequency ω of the full system at transmon flux Φ_T and chain flux Φ_C :

$$\tan \phi(\omega, \Phi_T, \Phi_C) = \frac{C_g - 2C_{\text{eff}}(\Phi_T, \omega)}{\sqrt{C_g(C_g + 4C_J)}} \frac{1}{\sqrt{\left(\frac{\omega_p(\Phi_C)}{\omega}\right)^2 - 1}}. \quad (\text{S28})$$

Here we give the derivation. We work in the thermodynamic limit where $N \rightarrow \infty$. This means that both matrices \hat{C} and \hat{J} (Eqs. (S32) and (S33)) become semi-infinite. Furthermore, the approximation discussed in the previous section eliminates the anharmonic term in H , and introduces four new non-zero matrix elements in \hat{J} , namely

$$\hat{J}_{L,L} = \hat{J}_{R,R} = E_S(\Phi_T), \quad (\text{S29})$$

$$\hat{J}_{R,L} = \hat{J}_{L,R} = -E_S(\Phi_T). \quad (\text{S30})$$

Making the flux-dependence of E_S explicit, we have from Eq. (S25)

$$E_S(\Phi_T) = E_{J,T}(\Phi_T) - \sqrt{E_{J,T}(\Phi_T) E_{C,T}/4}, \quad (\text{S31})$$

with $E_{J,T}(\Phi_T) = E_{J,T,\text{max}} |\cos(\pi\Phi_T/\Phi_0)|$. Explicitly the matrices \hat{C} and \hat{J} then read (see Eqs. (6) and (7) in the main text)

$$\hat{C} = \begin{pmatrix} C_0 & -C_{\text{sh},T} & 0 & 0 & 0 & 0 & \dots \\ -C_{\text{sh},T} & C_0 & -C_c & 0 & 0 & 0 & \dots \\ 0 & -C_c & C_1 & -C_J & 0 & 0 & \dots \\ 0 & 0 & -C_J & C_\Sigma & -C_J & 0 & \dots \\ \vdots & \vdots & \vdots & \ddots & \ddots & \ddots & \dots \end{pmatrix} \quad (\text{S32})$$

$$\hat{J} = \frac{\varphi_0^2}{L_J(\Phi_C)} \begin{pmatrix} 0 & 0 & 0 & 0 & 0 & 0 & \dots \\ 0 & 0 & 0 & 0 & 0 & 0 & \dots \\ 0 & 0 & 1 & -1 & 0 & 0 & \dots \\ 0 & 0 & -1 & 2 & -1 & 0 & \dots \\ \vdots & \vdots & \vdots & \ddots & \ddots & \ddots & \dots \end{pmatrix} + E_S(\Phi_T) \begin{pmatrix} 1 & -1 & 0 & 0 & 0 & 0 & \dots \\ -1 & 1 & 0 & 0 & 0 & 0 & \dots \\ 0 & 0 & 0 & 0 & 0 & 0 & \dots \\ 0 & 0 & 0 & 0 & 0 & 0 & \dots \\ \vdots & \vdots & \vdots & \vdots & \vdots & \vdots & \dots \end{pmatrix} \quad (\text{S33})$$

We now have a fully linear system. The phase shifts in Eq. (S28) are obtained by solving the classical equations of motion. We start by defining a vector with the superconducting phases in each island $\vec{\pi}^T = (\varphi_L, \varphi_R, \varphi_1, \varphi_2, \dots, \varphi_N)$. The equations of motion for the mode at frequency ω are given by

$$\hat{J}(\Phi_T, \Phi_C) \vec{\pi}_\omega = (\hbar\omega)^2 \frac{\hat{C}}{(2e)^2} \vec{\pi}_\omega. \quad (\text{S34})$$

The solution to the part of Eq. (S34) involving degrees of freedom in the chain can be taken as

$$\varphi_j = N(\omega) \cos [j\kappa(\omega, \Phi_C)a - \phi(\omega, \Phi_T, \Phi_C)] \quad \text{with } j = 1, 2, 3, 4 \dots \quad (\text{S35})$$

Here a is the length of the unit cell of the array, $N(\omega)$ a frequency dependent amplitude and $\kappa(\omega, \Phi_C)$ is the wave number of a wave that propagates in the chain with angular frequency ω . It can be obtained from the dispersion relation in Eq. (S2),

$$\kappa(\omega, \Phi_C) = \frac{2}{a} \operatorname{arccot} \sqrt{\left(\frac{4C_J}{C_g} + 1\right) \left[\left(\frac{\omega_p(\Phi_C)}{\omega}\right)^2 - 1\right]}, \quad (\text{S36})$$

where $\omega_p(\Phi_C) = 1/\sqrt{L_J(\Phi_C)(C_J + C_g/4)}$ is the plasma frequency of the chain. The phase shift $\phi(\omega, \Phi_T, \Phi_C)$ in Eq. (S35) is determined by the components of Eq. (S34) involving the transmon islands. They read

$$E_S(\Phi_T) (\varphi_L - \varphi_R) = \frac{(\hbar\omega)^2}{(2e)^2} (C_0\varphi_L - C_{\text{sh},T}\varphi_R), \quad (\text{S37})$$

$$E_S(\Phi_T) (\varphi_R - \varphi_L) = \frac{(\hbar\omega)^2}{(2e)^2} (-C_{\text{sh},T}\varphi_L - C_0\varphi_R - C_c\varphi_1), \quad (\text{S38})$$

$$E_S(\Phi_T) (\varphi_1 - \varphi_2) = \frac{(\hbar\omega)^2}{(2e)^2} (-C_{\text{sh},T}\varphi_R - C_1\varphi_1 - C_J\varphi_2). \quad (\text{S39})$$

Using Eq. (S37) and Eq. (S38) we eliminate φ_L and solve for φ_R in terms of φ_1 to obtain

$$\varphi_R = \frac{C_c \left[\frac{(\hbar\omega)^2}{(2e)^2} C_0 - E_S(\Phi_T) \right]}{(C_0 - C_{\text{sh},T}) \left[(C_0 + C_{\text{sh},T}) \frac{(\hbar\omega)^2}{(2e)^2} C_0 - 2E_S(\Phi_T) \right]} \varphi_1. \quad (\text{S40})$$

Substituting this into Eq. (S39) and using Eq. (S36) for $\kappa(\omega, \Phi_C)$ we obtain

$$\frac{C_g}{2[1 - \cos \kappa(\omega, \Phi_C)a]} (\varphi_1 - \varphi_2) = C_{\text{eff}}(\Phi_T, \omega) \varphi_1, \quad (\text{S41})$$

with

$$C_{\text{eff}}(\Phi_T, \omega) = C_1 - C_J - \frac{C_c^2 \left[\frac{(\hbar\omega)^2}{(2e)^2} C_0 - E_S(\Phi_T) \right]}{(C_0 - C_{\text{sh},T}) \left[(C_0 + C_{\text{sh},T}) \frac{(\hbar\omega)^2}{(2e)^2} C_0 - 2E_S(\Phi_T) \right]}. \quad (\text{S42})$$

Using the mode definition in Eq. (S35) for φ_1 and φ_2 in Eq. (S41) leads to

$$\tan \phi(\omega, \Phi_T, \Phi_C) = \left[1 - \frac{2C_{\text{eff}}(\Phi_T, \omega)}{C_g} \right] \tan \frac{\kappa(\omega, \Phi_C)a}{2}. \quad (\text{S43})$$

Finally, using again the expression in Eq. (S36) for $\kappa(\omega, \Phi_C)$ we obtain the expression for the phase shift ϕ as a function of the system parameters.

$$\tan \phi(\omega, \Phi_T, \Phi_C) = \left[1 - \frac{2C_{\text{eff}}(\Phi_T, \omega)}{C_g} \right] \sqrt{\frac{C_g}{C_g + 4C_J}} \frac{1}{\sqrt{\left(\frac{\omega_p(\Phi_C)}{\omega}\right)^2 - 1}}. \quad (\text{S44})$$

H. Link between the scattering phase shift and the relative frequency shift

In the main text we defined the relative frequency shift $\delta\phi_n$ in terms of the discrete mode frequencies of the full system (transmon plus finite chain of N nodes) at respective transmon fluxes Φ_T and $\Phi_0/2$. We repeat the definition here:

$$\delta\phi_n(\Phi_T, \Phi_C) = \pi \frac{\omega_n(\Phi_0/2, \Phi_C) - \omega_n(\Phi_T, \Phi_C)}{\omega_n(\Phi_0/2, \Phi_C) - \omega_{n-1}(\Phi_0/2, \Phi_C)}. \quad (\text{S45})$$

Here we relate this to the relative scattering phase shift $\delta\phi(\omega, \Phi_T, \Phi_C)$ for the infinite system (see Eq. 14 in the *Methods* section of the main text) by showing that

$$\delta\phi_n(\Phi_T, \Phi_C) = \delta\phi(\omega_n(\Phi_T, \Phi_C), \Phi_T, \Phi_C) + \mathcal{O}(N^{-1}). \quad (\text{S46})$$

For convenience we assume that island $N + 1$ is grounded. (The precise boundary condition becomes immaterial in the $N \rightarrow \infty$ limit.) Had the chain been open to the left of node 1, the eigenmodes would have been $\varphi_j \propto \cos(\kappa_n^0 a j)$, $j \in 1, 2, 3, \dots, N$ with wave numbers given by $\kappa_n^0 = (n - 1/2)\pi/Na$ with $n \in 1, 2, 3, \dots, N$. In the presence of the transmon to the left of chain node 1, the eigenmodes inside the chain change to $\cos(\kappa_n a j - \phi_n)$. Here ϕ_n is the additional phase introduced by the transmon. Now the κ_n depend on ϕ_n too. Assuming the boundary conditions that the nodes to the left of transmon island L and to the right of chain island N are grounded, they are given by

$$\kappa_n a = \frac{(n - \frac{1}{2})\pi}{N} + \frac{\phi_n}{N} = \kappa_n^0 a + \frac{\phi_n}{N}. \quad (\text{S47})$$

The modes of the system follow a dispersion relation $\omega_n(\Phi_T, \Phi_C) = \omega(\Phi_C, \kappa_n)$. The notation must be understood as follows: $\omega_n(x, y)$ and $\omega(x, y)$ denote distinct functions. The two arguments of the former refer to respectively the flux in a transmon and in a chain SQUID, and for given fluxes, the function assumes the value of the frequency of system mode n . The first argument of the latter function $\omega(x, y)$ refers to the flux in a chain SQUID, while the second argument refers to the unquantized wave number of a mode in the infinite chain. The function evaluates to the frequency corresponding to the given wave number (which does not depend on the transmon flux). For sufficiently large N we can expand the dispersion relation around $\kappa_n^0 a$

$$\omega_n(\Phi_T, \Phi_C) = \omega(\Phi_C, \kappa_n^0) + \frac{\phi_n(\Phi_T, \Phi_C)}{N} \frac{\partial\omega(\Phi_C, \kappa)}{\partial(\kappa a)} \Big|_{\kappa=\kappa_n^0}, \quad (\text{S48})$$

with corrections of order N^{-2} . The dependence on the transmon and chain fluxes is included. Similarly, we can expand $\omega_{n-1}(\Phi_T, \Phi_C)$ around $\kappa_{n-1}^0 a$ to obtain

$$\omega_{n-1}(\Phi_T, \Phi_C) = \omega_n(\Phi_T, \Phi_C) - \frac{\pi}{N} \frac{\partial\omega(\Phi_C, \kappa)}{\partial(\kappa a)} \Big|_{\kappa=\kappa_n^0}. \quad (\text{S49})$$

Here we made use of the fact that $\phi_n - \phi_{n-1} = \mathcal{O}(N^{-1})$. Therefore we can set $\phi_{n-1} = \phi_n$ introducing an error of $\mathcal{O}(N^{-2})$ which can be ignored for large N . We can now obtain the terms in Eq. (S45),

$$\omega_n(\Phi_0/2, \Phi_C) = \omega(\Phi_C, \kappa_n^0) + \frac{\phi_n(\Phi_0/2, \Phi_C)}{N} \frac{\partial\omega(\Phi_C, \kappa)}{\partial(\kappa a)} \Big|_{\kappa=\kappa_n^0} \quad (\text{S50})$$

$$\omega_n(\Phi_T, \Phi_C) = \omega(\Phi_C, \kappa_n^0) + \frac{\phi_n(\Phi_T, \Phi_C)}{N} \frac{\partial\omega(\Phi_C, \kappa)}{\partial(\kappa a)} \Big|_{\kappa=\kappa_n^0} \quad (\text{S51})$$

$$\omega_{n-1}(\Phi_0/2, \Phi_C) = \omega_n(\Phi_0/2, \Phi_C) - \frac{\pi}{N} \frac{\partial\omega(\Phi_C, \kappa)}{\partial(\kappa a)} \Big|_{\kappa=\kappa_n^0}. \quad (\text{S52})$$

Substituting this into Eq. (S45), and noting that $\phi_n(\Phi_T, \Phi_C) = \phi(\omega_n(\Phi_T, \Phi_C), \Phi_T, \Phi_C)$, we obtain Eq. (S46).

I. Relation between the Phase Shift and the impurity response function

To elaborate the link between the local impurity response function and the phase shift induced by the transmon qubit, we define three spectral densities

$$A_1(\omega) = \frac{2E_S(\Phi_T)}{\omega_T} \text{Re} \int_0^\infty \frac{dt}{2\pi} e^{i\omega t} \langle [\hat{\varphi}_T(t), \hat{\varphi}_T(0)] \rangle, \quad (\text{S53})$$

$$A_2(\omega) = -\text{Im} \int_0^\infty \frac{dt}{2\pi} e^{i\omega t} \langle [\hat{\varphi}_T(t), \hat{n}_T(0)] \rangle, \quad (\text{S54})$$

$$A_3(\omega) = \frac{2\omega_T}{E_S(\Phi_T)} \text{Re} \int_0^\infty \frac{dt}{2\pi} e^{i\omega t} \langle [\hat{n}_T(t), \hat{n}_T(0)] \rangle, \quad (\text{S55})$$

corresponding to the phase-phase, phase-charge and charge-charge response of the transmon up to constant prefactors. In order to calculate these spectral densities we turn to the quantum mechanical problem (In the previous section, we could compute the phase shift by solving the classical equations of motion). With each mode ω we associate canonical bosonic operators b_ω and b_ω^\dagger . These are related to the charge operator \hat{n}_j and phase operator $\hat{\varphi}_j$ for each of the islands as

$$\hat{\varphi}_j = \frac{-i}{\sqrt{2}} \int_0^{\omega_p(\Phi_C)} d\omega \varphi_j(\omega) (b_\omega - b_\omega^\dagger), \quad (\text{S56})$$

$$\hat{n}_j = \frac{1}{\sqrt{2}} \int_0^{\omega_p(\Phi_C)} \frac{d\omega}{\omega} \sum_{l=L,R,1,2,\dots} \hat{J}(\Phi_T, \Phi_C)_{j,l} \varphi_l(\omega) (b_\omega + b_\omega^\dagger), \quad (\text{S57})$$

where the profile $\varphi_j(\omega)$ is normalized such that

$$\sum_{j=L,R,1,2,\dots} \varphi_j(\omega) \hat{J}(\Phi_T, \Phi_C)_{j,l} \varphi_l(\omega') = \omega \delta(\omega - \omega'). \quad (\text{S58})$$

The normalization constant in Eq. (S35) is thus set to

$$N_\omega = \sqrt{\frac{\hbar\omega}{\pi E_J(\Phi_C)[1 - \cos \kappa(\omega, \Phi_C)]} \frac{\partial \kappa(\omega, \Phi_C)}{\partial \omega}}. \quad (\text{S59})$$

From the definition of \hat{n}_T and $\hat{\varphi}_T$ (see the text below Eq. 7 in the *Methods* section of the main text) follows

$$\hat{n}_T = (\hat{n}_R - \hat{n}_L)/2 = \frac{1}{\sqrt{2}} \int_0^{\omega_p(\Phi_C)} d\omega \frac{E_S(\Phi_C)}{\omega} [\varphi_R(\omega) - \varphi_L(\omega)] (b_\omega + b_\omega^\dagger), \quad (\text{S60})$$

$$\hat{\varphi}_T = \hat{\varphi}_R - \hat{\varphi}_L = \frac{-i}{\sqrt{2}} \int_0^{\omega_p(\Phi_C)} d\omega [\varphi_R(\omega) - \varphi_L(\omega)] (b_\omega - b_\omega^\dagger). \quad (\text{S61})$$

Explicitly, we find:

$$\varphi_R(\omega) - \varphi_L(\omega) = N_\omega \frac{C_c \omega^2 / (2e)^2}{(C_0 + C_{\text{sh},T}) \omega^2 / (2e)^2 - 2E_S(\Phi_T)} \cos \phi(\omega, \Phi_T, \Phi_C). \quad (\text{S62})$$

In the Heisenberg picture $b_\omega(t) = e^{i\omega t} b_\omega$ and $b_\omega^\dagger(t) = e^{-i\omega t} b_\omega^\dagger$. Using this to calculate the spectral densities $A_j(\omega)$ for $\omega > 0$ we obtain

$$A_1(\omega) = \frac{E_S(\Phi_T)}{\omega_T} [\varphi_R(\omega) - \varphi_L(\omega)]^2, \quad (\text{S63})$$

$$A_2(\omega) = \frac{E_S(\Phi_T)}{\omega} [\varphi_R(\omega) - \varphi_L(\omega)]^2, \quad (\text{S64})$$

$$A_3(\omega) = \frac{E_S(\Phi_T) \omega_T}{\omega^2} [\varphi_R(\omega) - \varphi_L(\omega)]^2 \quad (\text{S65})$$

Now we compare the three correlation functions with the frequency derivative of $\delta\phi(\omega, \Phi_T, \Phi_C) = \phi(\omega, \Phi_T, \Phi_C) - \phi(\omega, \Phi_0/2, \Phi_C)$ with $\phi(\omega, \Phi_T, \Phi_C)$ given in Eq. (S28). In Fig. S12 we plot the four curves. We see that the four curves overlap around the transmon frequency ω_T . This means that the width and the center frequency obtained from the scattering phase shift are good estimations of the real width Γ_T and frequency ω_T of the transmon.

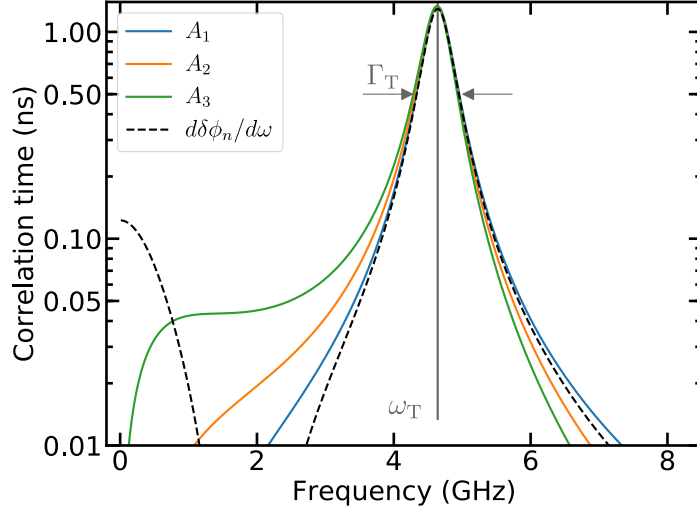


FIG. S12. **Connection between phase shifts and qubit dissipation.** Comparison between the three correlation functions and the energy derivative of the phase shift.

J. Breakdown of the rotating wave approximation

In this section, we investigate the applicability of the rotating wave approximation (RWA), a common technique for analysing the light-matter interaction at sufficiently weak coupling. The regime in which the light-matter coupling is so large that this approximation becomes inaccurate, is referred to as ultra-strong coupling. We will find that indeed, the RWA leads to errors of a few percent for our device.

To set up the RWA, we have to identify the harmonic oscillator basis that diagonalizes the (finite) chain part of the Hamiltonian. For this purpose, it is convenient to define $N \times N$ matrices $\hat{C}_{\text{chain}}^{-1}$ and $\hat{L}_{\text{chain}}^{-1}$ with entries

$$[\hat{C}_{\text{chain}}^{-1}]_{jk} = [\hat{C}^{-1}]_{jk}, \quad [\hat{L}_{\text{chain}}^{-1}]_{jk} = [\hat{J}]_{jk}/\varphi_0^2, \quad j, k = 1, 2, \dots, N, \quad (\text{S66})$$

i.e. $\hat{C}_{\text{chain}}^{-1}$ and $\varphi_0^2 \hat{L}_{\text{chain}}^{-1}$ are the lower right $N \times N$ blocks of respectively the inverse of the full $(N+2) \times (N+2)$ capacitance matrix \hat{C} , and of the full $(N+2) \times (N+2)$ Josephson matrix \hat{J} . We then define an $N \times N$ matrix $\hat{\Pi}_{\text{chain}}$ and a positive definite diagonal matrix $\hat{\omega}_{\text{chain}}$ such that the columns of $\hat{\Pi}_{\text{chain}}$ contain the eigenvectors of $\hat{C}_{\text{chain}}^{-1} \hat{L}_{\text{chain}}^{-1}$ while the diagonal entries of $(\hat{\omega}_{\text{chain}})^2$ are the corresponding eigenvalues, i.e.

$$\hat{C}_{\text{chain}}^{-1} \hat{L}_{\text{chain}}^{-1} \hat{\Pi}_{\text{chain}} = \hat{\Pi}_{\text{chain}} (\hat{\omega}_{\text{chain}})^2. \quad (\text{S67})$$

Since the eigenvalues are real, we can and will choose the entries of $\hat{\Pi}_{\text{chain}}$ to be real as well. This definition determines each column of $\hat{\Pi}_{\text{chain}}$ up to a normalization constant. We fix these constants by demanding that

$$\varphi_0^2 \sum_{jk} [\hat{L}_{\text{chain}}^{-1}]_{jk} [\hat{\Pi}_{\text{chain}}]_{jl} [\hat{\Pi}_{\text{chain}}]_{kl} = \hbar [\omega_{\text{chain}}]_l, \quad (\text{S68})$$

where $[\omega_{\text{chain}}]_l$ is the l 'th diagonal entry of $\hat{\omega}_{\text{chain}}$. We also define a matrix

$$\hat{\Xi}_{\text{chain}} = \varphi_0^2 \hat{L}_{\text{chain}}^{-1} \hat{\Pi}_{\text{chain}} \hat{\omega}_{\text{chain}}^{-1} / \hbar. \quad (\text{S69})$$

It is easy to verify that the row l of $\hat{\Xi}_{\text{chain}}^T$ contains the left-eigenvector of $\hat{C}_{\text{chain}}^{-1} \hat{L}_{\text{chain}}^{-1}$ that is associated with eigenvalue $([\omega_{\text{chain}}]_l)^2$. As a result $\hat{\Xi}_{\text{chain}}^T \hat{\Pi}_{\text{chain}}$ is guaranteed to be a diagonal matrix. Furthermore, due to the normalization condition (S68) we chose for $\hat{\Pi}_{\text{chain}}$, the diagonal entries of $\hat{\Xi}_{\text{chain}}^T \hat{\Pi}_{\text{chain}}$ are all equal to unity. Thus

$$\hat{\Xi}_{\text{chain}}^T = \hat{\Pi}_{\text{chain}}^{-1}. \quad (\text{S70})$$

We now define N operators

$$\hat{b}_{\text{chain},k} = \frac{1}{\sqrt{2}} \sum_{j=1}^N \left\{ \hat{n}_j [\hat{\Pi}_{\text{chain}}]_{jk} + i \hat{\varphi}_j [\hat{\Xi}_{\text{chain}}]_{jk} \right\}. \quad (\text{S71})$$

Owing to (S70) and the fact that $[\hat{n}_j, \hat{\varphi}_k] = i \delta_{j,k}$, the operators $\hat{b}_{\text{chain},k}$, $k = 1, 2, \dots, N$ are bosonic annihilation operators, i.e. $[\hat{b}_{\text{chain},j}, \hat{b}_{\text{chain},k}] = 0$ and $[\hat{b}_{\text{chain},j}, \hat{b}_{\text{chain},k}^\dagger] = \delta_{j,k}$. Furthermore, for the chain part of the Hamiltonian we obtain

$$\begin{aligned} H_{\text{chain}} &= \frac{1}{2} \sum_{j,k=1}^N \left\{ (2e)^2 [\hat{C}_{\text{chain}}^{-1}]_{jk} \hat{n}_j \hat{n}_k + \varphi_0^2 [\hat{L}_{\text{chain}}^{-1}]_{jk} \hat{\varphi}_k \hat{\varphi}_j \right\} \\ &= \hbar \sum_{j=1}^N [\omega_{\text{chain}}]_j \left(\hat{b}_{\text{chain},j}^\dagger \hat{b}_{\text{chain},j} - \frac{1}{2} \right). \end{aligned} \quad (\text{S72})$$

For the term in the Hamiltonian that couples the transmon to the chain, we find

$$\begin{aligned} H_{\text{coupling}} &= \hat{n}_{\text{T}} \sum_{j=1}^N \nu_j \hat{n}_j \\ &= \frac{1}{\sqrt{2}} \hat{n}_{\text{T}} \sum_{k=1}^N g_k \left(\hat{b}_{\text{chain},k} + \hat{b}_{\text{chain},k}^\dagger \right) \end{aligned} \quad (\text{S73})$$

where

$$g_k = \sum_{j=1}^N \nu_j [\hat{\Xi}_{\text{chain}}]_{jk}. \quad (\text{S74})$$

A standard way to proceed from here is to truncate the full Hilbert space of the transmon to the subspace spanned by two lowest energy eigenstates $|0_{\text{T}}\rangle$ and $|1_{\text{T}}\rangle$ of the isolated transmon Hamiltonian (S13). This leads to a Hamiltonian of the Jaynes-Cummings type, ubiquitous in Quantum Optics. At sufficiently weak coupling, the expectation is that this should be accurate for studying the situation where a near-resonant excitation from the chain induces a transition between the ground and first excited states of the transmon. The operator \hat{n}_{T} is replaced by

$$\hat{n}_{\text{T}} \simeq \langle 0_{\text{T}} | \hat{n}_{\text{T}} | 1_{\text{T}} \rangle \{ |0_{\text{T}}\rangle \langle 1_{\text{T}}| + |1_{\text{T}}\rangle \langle 0_{\text{T}}| \}, \quad (\text{S75})$$

where we've chosen the overall phases of $|0_{\text{T}}\rangle$ and $|1_{\text{T}}\rangle$ such that $\langle 0_{\text{T}} | \hat{n}_{\text{T}} | 1_{\text{T}} \rangle$ is real.

Alternatively, a more controlled way to proceed is to make the self-consistent harmonic approximation (SCHA) (see Sec. F), which we have shown to be well-justified, and to express \hat{n}_{T} in terms of the resulting bosonic transmon operators [see Eq. (S20)], i.e.

$$\hat{n}_{\text{T}} = \frac{1}{\sqrt{2}} \left(\frac{E_{\text{C,T}}}{E_{\text{S}}} \right)^{1/4} (B + B^\dagger). \quad (\text{S76})$$

After the SCHA, the Hamiltonian becomes quadratic, and no further approximations are required. We will however still consider the effect of making the RWA on this quadratic Hamiltonian, in order to assess whether or not the assumptions underpinning the RWA are valid in our device.

The RWA approximation now involves dropping the transmon-chain coupling terms in which the transmon (in the unperturbed basis) is excited while a boson is emitted into the chain, or the transmon is de-excited while a boson is absorbed from the chain. We adopt the standard nomenclature and refer to the dropped terms as ‘‘counter-rotating’’ (based on their time-dependence in the Dirac picture). Depending on whether this approximation is made in conjunction with truncating the transmon Hilbert space or with the SCHA, we either obtain an RWA Hamiltonian

$$\begin{aligned} H_{\text{RWA},1} &= (E_{1,\text{T}} - E_{0,\text{T}}) |1_{\text{T}}\rangle \langle 1_{\text{T}}| + \sum_{n=1}^N \hbar [\omega_{\text{chain}}]_n \hat{b}_{\text{chain},n}^\dagger \hat{b}_{\text{chain},n} \\ &+ \frac{1}{\sqrt{2}} \langle 0_{\text{T}} | \hat{n}_{\text{T}} | 1_{\text{T}} \rangle \sum_{k=1}^N g_k \left(|0_{\text{T}}\rangle \langle 1_{\text{T}}| \hat{b}_{\text{chain},k} + |1_{\text{T}}\rangle \langle 0_{\text{T}}| \hat{b}_{\text{chain},k}^\dagger \right), \end{aligned} \quad (\text{S77})$$

or

$$H_{\text{RWA},2} = \omega_{\text{T}} B^\dagger B + \sum_{n=1}^N \hbar[\omega_{\text{chain}}]_n \hat{b}_{\text{chain},n}^\dagger \hat{b}_{\text{chain},n} + \frac{1}{2} \left(\frac{E_{\text{C,T}}}{E_{\text{S}}} \right)^{1/4} \sum_{k=1}^N g_k \left(B^\dagger \hat{b}_{\text{chain},k} + \hat{b}_{\text{chain},k}^\dagger B \right). \quad (\text{S78})$$

For both Hamiltonians, the ground state is trivial: the transmon is in its unperturbed ground state, and there are no bosonic excitations in the chain. We measure energy relative to this ground state. Both Hamiltonians leave invariant the subspace spanned by states in which there are no bosons in the chain, while the transmon is in its unperturbed first excited state, or there is one boson in the chain while the transmon is in its unperturbed ground state. The excited states relevant for spectroscopy at low driving power are found by diagonalizing the RWA Hamiltonians in this subspace.

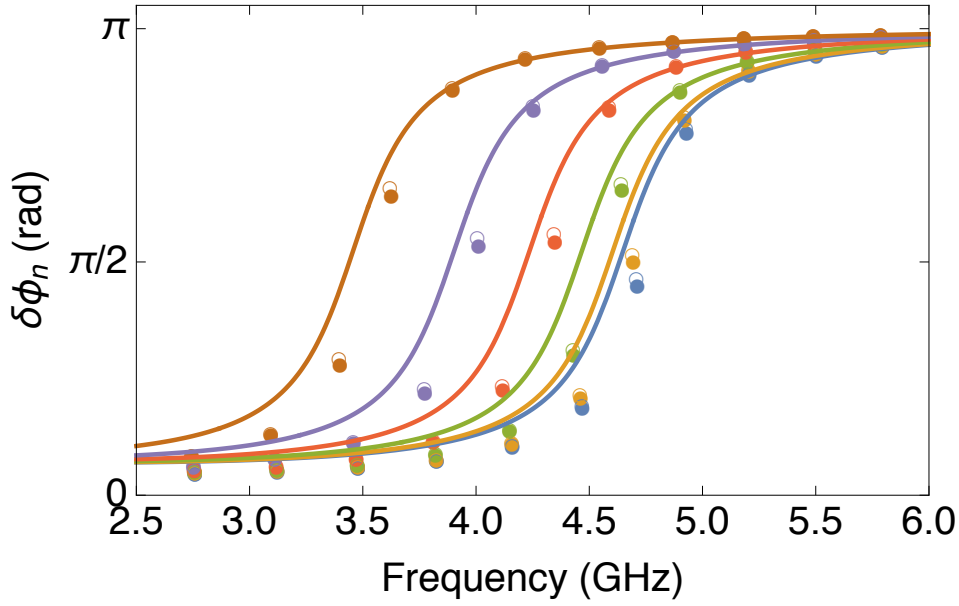


FIG. S13. **Deviations from the microscopic model under the RWA assumption.** Curves show the analytical formula for the relative frequency shift (Eq. 14 in the main text). Open circles show the corresponding result calculated using $H_{\text{RWA},1}$ and closed circles the result calculated using $H_{\text{RWA},2}$. In all cases the system parameters were taken as in Table 1 of the main text. The flux Φ_{C} through chain SQUIDS was held fixed at zero. Results for six different fluxes $\Phi_{\text{T}} \in [0, 0.3\Phi_0]$ through the transmon SQUID are shown.

In Figure S13 we compare the relative frequency shift (Eq. 1 in the main text) predicted by $H_{\text{RWA},1}$ and $H_{\text{RWA},2}$ to the analytical SCHA formula (Eq. 14 in the main text) derived for an infinite chain. We have also computed SCHA results for the finite chain of 4700 islands, and found that they lie on top of the infinite chain curves. We omit them from the figure to avoid clutter. We note that $H_{\text{RWA},1}$ and $H_{\text{RWA},2}$ give very similar results. This is consistent with our claim that at low energies, the SCHA Hamiltonian from which $H_{\text{RWA},2}$ derives, is a good approximation to the full Hamiltonian from which $H_{\text{RWA},1}$ is derived. We ascribe the small difference between results for $H_{\text{RWA},1}$ and $H_{\text{RWA},2}$ to the truncation by hand in $H_{\text{RWA},1}$ of the transmon Hilbert space to two states. (No such by-hand truncation was required in $H_{\text{RWA},2}$.) If we fit an arctan line shape (Eq. 18 in the main text) to the SCHA curves in the figure, we find that the transmon resonance occurs at a frequency within about 0.01 GHz from \hbar^{-1} times the energy difference between the ground and first excited states of the isolated transmon. Using the same procedure on the relative frequency shift predicted by either $H_{\text{RWA},1}$ or $H_{\text{RWA},2}$ on the other hand, gives a resonance frequency that is ~ 0.1 GHz higher than \hbar^{-1} times the ground to first excitation energy of the isolated transmon. We conclude that the RWA approximation is not quantitatively accurate, producing an error of between 2% and 5% for the transmon

resonance frequency. This signals that our device indeed operates in the ultra-strong light-matter coupling regime.

- ¹ N. Masluk, I. Pop, A. Kamal, Z. Mineev, and M. Devoret, *Physical Review Letters* **109**, 137002 (2012).
- ² T. Weiszl, *Quantum phase and charge dynamics in Josephson junction chains*, Ph.D. thesis, Université Joseph Fourier (2014).
- ³ T. Weiszl, B. Küng, E. Dumur, A. K. Feofanov, I. Matei, C. Naud, O. Buisson, F. W. J. Hekking, and W. Guichard, *Physical Review B* **92**, 104508 (2015).
- ⁴ A. Fay, *Couplage variable entre un qubit de charge et un qubit de phase*, Ph.D. thesis, Université Joseph Fourier (2008).
- ⁵ D. A. Frickey, *IEEE Transactions on microwave theory and techniques* **42** (1994).
- ⁶ D. Pozar, *Microwave Engineering*, edited by J. Wiley and Sons (John Wiley and Sons, 2005).
- ⁷ J. Koch, T. M. Yu, J. Gambetta, A. A. Houck, D. I. Schuster, J. Majer, A. Blais, M. H. Devoret, S. M. Girvin, and R. J. Schoelkopf, *Physical Review A* **76**, 042319 (2007).